

Ensemble cryoEM elucidates the mechanism of insulin capture and degradation by human insulin degrading enzyme

Zhening Zhang^{1†}, Wenguang G Liang^{2†}, Lucas J Bailey³, Yong Zi Tan^{1,4}, Hui Wei¹, Andrew Wang², Mara Farcasanu², Virgil A Woods⁵, Lauren A McCord², David Lee⁵, Weifeng Shang⁶, Rebecca Deprez-Poulain⁷, Benoit Deprez⁷, David R Liu⁸, Akiko Koide^{9,10,11}, Shohei Koide^{9,10,11}, Anthony A Kossiakoff³, Sheng Li^{5*}, Bridget Carragher^{1,4*}, Clinton S Potter^{1,4*}, Wei-Jen Tang^{2*}

¹National Resource for Automated Molecular Microscopy, Simons Electron Microscopy Center, New York Structural Biology Center, New York, United States; ²Ben-May Institute for Cancer Research, The University of Chicago, Chicago, United States; ³Department of Biochemistry and Molecular Biology, The University of Chicago, Chicago, United States; ⁴Department of Biochemistry and Molecular Biophysics, Columbia University, New York, United States; ⁵Department of Medicine, University of California, San Diego, La Jolla, United States; ⁶BioCAT, Argonne National Laboratory, Illinois, United States; ⁷Univ. Lille, INSERM, Institut Pasteur de Lille, Lille, France; ⁸Department of Chemistry and Chemical Biology, Harvard University, Cambridge, United States; ⁹Perlmutter Cancer Center, New York University School of Medicine, New York, United States; ¹⁰New York University Langone Medical Center, New York University School of Medicine, New York, United States; ¹¹Department of Biochemistry and Molecular Pharmacology, New York University School of Medicine, New York, United States

***For correspondence:**

Corresponding authorss4li@ucsd.edu (SL);
bcarr@nysbc.org (BC);
cpotter@nysbc.org (CSP);
wtang@bsd.uchicago.edu (W-JT)

[†]These authors contributed equally to this work

Competing interests: The authors declare that no competing interests exist.

Funding: See page 21

Received: 15 November 2017

Accepted: 28 March 2018

Published: 29 March 2018

Reviewing editor: Sriram Subramaniam, National Cancer Institute, United States

© Copyright Zhang et al. This article is distributed under the terms of the [Creative Commons Attribution License](https://creativecommons.org/licenses/by/4.0/), which permits unrestricted use and redistribution provided that the original author and source are credited.

Abstract Insulin degrading enzyme (IDE) plays key roles in degrading peptides vital in type two diabetes, Alzheimer's, inflammation, and other human diseases. However, the process through which IDE recognizes peptides that tend to form amyloid fibrils remained unsolved. We used cryoEM to understand both the apo- and insulin-bound dimeric IDE states, revealing that IDE displays a large opening between the homologous ~55 kDa N- and C-terminal halves to allow selective substrate capture based on size and charge complementarity. We also used cryoEM, X-ray crystallography, SAXS, and HDX-MS to elucidate the molecular basis of how amyloidogenic peptides stabilize the disordered IDE catalytic cleft, thereby inducing selective degradation by substrate-assisted catalysis. Furthermore, our insulin-bound IDE structures explain how IDE processively degrades insulin by stochastically cutting either chain without breaking disulfide bonds. Together, our studies provide a mechanism for how IDE selectively degrades amyloidogenic peptides and offers structural insights for developing IDE-based therapies.

DOI: <https://doi.org/10.7554/eLife.33572.001>

Introduction

Insulin degrading enzyme (IDE) is an evolutionarily conserved, M16 family metalloprotease that controls diverse biological functions in model organisms such as mating and cell division in budding

yeast and growth in fruit flies (Adames et al., 1995; Fujita et al., 1994; Galagovsky et al., 2014; Tang, 2016). IDE is ubiquitously expressed in all tissues and can be found in almost all subcellular compartments, despite being made as a cytosolic protein (Tang, 2016; Tundo et al., 2017). IDE can effectively degrade insulin, amylin, and glucagon, pancreatic hormones that control blood glucose levels, as well as amyloid β ($A\beta$), a peptide implicated in Alzheimer's disease (Duckworth et al., 1998; Kurochkin et al., 2018; Pivovarova et al., 2016; Tang, 2016; Tundo et al., 2017). Defects in IDE alter the progression of type two diabetes mellitus and Alzheimer's disease in rodents and are linked to these diseases in humans (Farris et al., 2003; Farris et al., 2004; Fuchsberger et al., 2016; Pivovarova et al., 2016; Tang, 2016; Tundo et al., 2017). Two IDE-specific inhibitors improve glucose tolerance (Durham et al., 2015; Maianti et al., 2014) and IDE overexpression reduces $A\beta$ load in mice (Leissring et al., 2003), making this enzyme a promising therapeutic target (Kurochkin et al., 2018; Pivovarova et al., 2016; Tang, 2016; Tundo et al., 2017).

Crystallographic and biochemical studies have provided the framework for IDE substrate recognition (Guo et al., 2010; Malito et al., 2008a; Malito et al., 2008b; Manolopoulou et al., 2009; Noinaj et al., 2011; Ren et al., 2010; Shen et al., 2006; Tang, 2016). IDE is a 110 kDa zinc metalloprotease that readily dimerizes in solution ($K_d \approx 10$ nM) (Li et al., 2006). IDE has at least two major conformational states in its catalytic cycle; open-state IDE captures substrates and releases products while closed-state IDE performs catalysis (Figure 1A). Thus far, all crystal structures of dimeric IDE are in the closed state. Within the IDE dimer, each IDE subunit consists of ~ 55 kDa N- and C-terminal domains, IDE-N and IDE-C (Figure 1B). Together, these domains form an enclosed, sizable catalytic chamber, the size of which explains why IDE prefers to degrade peptides that are less than 80 amino acid long (Figure 1B). Various substrate-bound IDE structures reveal that the high selectivity of IDE is partly achieved by the specific interactions between the IDE catalytic chamber and substrate via size and charge complementarity (Guo et al., 2010; Malito et al., 2008b; Manolopoulou et al., 2009; Ralat et al., 2011; Ren et al., 2010; Shen et al., 2006). The formation of cross- β -sheet between an exposed β -strand in the unfolded substrate and the catalytic cleft in conjunction with the anchoring of the substrate's N-terminus of substrate to a site that is ~ 30 Å away from the catalytic zinc ion explains how IDE selectively cleaves the exposed β -strand distal to the N-terminus of the targeted peptides in a stochastic manner (Shen et al., 2006).

Until now, structures of open and insulin-bound state IDE, two key conformations vital for the IDE catalytic cycle, have remained unsolved (Figure 1A and C). In closed-state IDE, substrate cannot enter into the catalytic chamber of IDE and the cleaved products cannot exit. Thus, IDE needs to undergo a significant open-closed transition during its catalytic cycle. In addition to contributing to an understanding of how IDE captures its substrate and releases its reaction products, the structure of open-state IDE can provide the insight into how the open-closed transition of IDE facilitates the unfolding of its substrates prior to the cleavage reaction as well as how IDE conducts its non-proteolytic roles, for example, regulating proteasome activity and preventing amyloid fibril formation of α -synuclein (Sharma et al., 2015; Tang, 2016). The IDE-insulin interaction represents a unique challenge of how IDE interacts with its substrates. Insulin consists of A and B chains that are held together by two inter-molecular disulfide bonds. IDE processively degrades insulin into two pieces without breaking these disulfide bonds (Figure 1A) (Manolopoulou et al., 2009). The previously reported crystal structure of insulin-bound IDE reveals how insulin is partially unfolded inside the catalytic chamber of IDE, the first step in the unfolding and degradation of insulin by IDE (Manolopoulou et al., 2009) (Figure 1C). However, the structure of IDE in complex with the fully unfolded insulin prior to the processive cleavage of insulin has remained unsolved.

Amyloidogenic peptides such as $A\beta$ can form highly toxic oligomers/fibrils, leading to many human disorders (Chiti and Dobson, 2006; Eisenberg and Jucker, 2012; Merlini and Bellotti, 2003). A salient feature of many amyloidogenic peptides is their high propensity to unfold, resulting in exposed β -strands that together form cross- β -sheets and then amyloid fibrils (Eisenberg and Jucker, 2012; Fitzpatrick et al., 2017; Lu et al., 2013). Nucleation to form low-molecular-weight oligomers is a key rate limiting step in the formation of amyloid fibrils (Merlini and Bellotti, 2003). IDE selectively degrades certain amyloidogenic peptides, preventing amyloid fibril formation (Kurochkin, 2001; Malito et al., 2008a). IDE achieves this by cutting only the monomeric form of these peptides and cleaving at sites located at the β -strand vital for cross- β -sheet formation (Malito et al., 2008a; Tang, 2016). Based on the absence of electron density for the catalytic zinc ion-containing IDE door subdomain in a previously reported Fab1-bound IDE crystal structure, we have put forth a

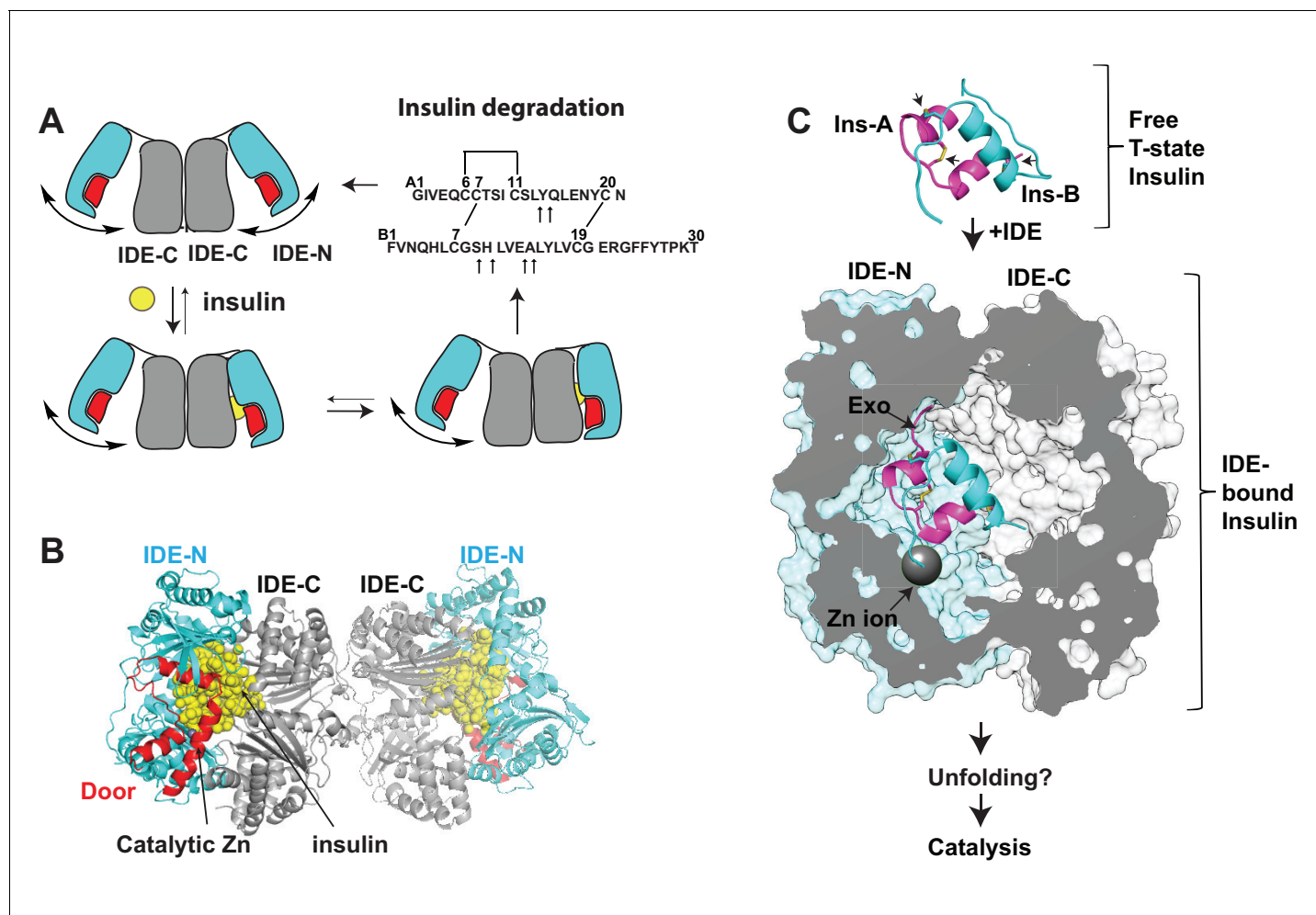


Figure 1. Summary of key unsolved IDE structures. (A) Schematic diagram for the catalytic cycle of IDE. IDE is dimerized via the interaction of IDE-C domains. The open-closed transition of IDE dimer is postulated to be mediated by the rigid-body motion between IDE-N and IDE-C. The binding of substrate, e.g., insulin shifts the equilibrium from favoring the open-state IDE to predominantly closed-state IDE. Until now, the structure of open-state IDE has not been determined. (B) Ribbon representation of IDE dimer (PDB code: 2WBY). IDE-N and IDE-C are colored in cyan and grey, respectively. The IDE door subdomain that contains the catalytic zinc ion is highlighted in red and the partially unfolded insulin entrapped inside the catalytic chamber of IDE is colored in yellow. (C) The key conformational switches required for insulin unfolding and degradation by IDE. Insulin A and B chains in ribbon representation are colored in magenta and cyan, respectively. Top: Insulin alone structure where the intra- and inter-molecular disulfide bonds are marked by arrows. Middle: IDE-bound insulin structure that contains partially unfolded insulin (PDB code: 2WBY). The N-terminus binding exosite (Exo) and catalytic zinc ion are marked by arrows. Until now, the structure of IDE in complex with the fully unfolded or cleaved insulin is not determined. DOI: <https://doi.org/10.7554/eLife.33572.002>

hypothesis that IDE uses substrate-assisted catalysis to recognize amyloidogenic peptides (McCord *et al.*, 2013). Upon substrate capture, the open-closed transition of IDE causes amyloidogenic peptides to unfold. The resulting exposed β -strand then binds and stabilizes the catalytic cleft within the IDE door subdomain, leading to stochastic cleavage of these peptides. This hypothesis could explain how IDE uses substrate-induced stabilization of the IDE catalytic site to selectively degrade amyloidogenic peptides. However, this hypothesis has not been formally tested. Thus, the molecular basis for the recognition of amyloidogenic peptides by IDE remains unsolved.

Recent advances in cryogenic electron microscopy (cryoEM) have profoundly transformed structural biology, making it possible to obtain near atomic resolution 3D structures that are otherwise difficult to achieve by crystallography (Henderson, 2015; Merk *et al.*, 2016). Here, we report cryoEM structures of apo and unfolded insulin-bound human IDE, which is recalcitrant to crystallography. Hydrogen-deuterium exchange coupled with mass spectrometry (HDX-MS) and small angle

X-ray scattering (SAXS) have recently become widely used techniques to characterize the high-order structure of proteins and protein complexes under physiological conditions in solution, nicely complement high-resolution techniques such as crystallography and cryoEM (Blanchet and Svergun, 2013; Marciano et al., 2014; Putnam et al., 2007; Ward et al., 2013; Wei et al., 2014). We integrate all four aforementioned structure methods to elucidate the molecular basis of how IDE captures, unfolds, and degrades its substrates and how IDE recognizes amyloidogenic peptides.

Results

Fab-assisted cryoEM of human IDE

Because IDE in the open conformation has proved recalcitrant to crystallization, we explored the use of cryoEM to study these structures. While IDE readily dimerizes ($K_d = 10$ nM), the dimer's overall size (220 kDa), pseudo two-fold symmetry and conformational heterogeneity made it challenging for cryoEM (data not shown). We addressed these issues by using Fab-assisted cryoEM (Kim et al., 2015; Lyumkis et al., 2013; Wu et al., 2012). To identify Fabs that bind IDE tightly, we screened a phage-display synthetic Fab library constructed using 'restricted chemical diversity' where positions randomized within the complementarity determining regions are biased toward amino acids enriched in antibody paratopes (Miller et al., 2012). This allowed rapid identification of eighteen high-affinity IDE binding Fabs without immunization. Fab_{H11} was chosen because it bound IDE tightly (~1 nM) and only slightly increased IDE activity (Figure 2—figure supplement 1A–C). We then rigidified the elbow region between the heavy and light chain of Fab_{H11}, which has improved the resolution of several structures that used Fab as the crystallization chaperone (Bailey et al., 2018). The resulting molecule, Fab_{H11-E}, was then used to determine an X-ray structure of Fab_{H11-E}-bound IDE at 3.8 Å resolution ($R/R_{free} = 22/27\%$, Supplementary file 1). This structure reveals the binding epitope of this Fab to IDE (Figure 2A and B). The tight binding between IDE and Fab_{H11-E} is mediated by a network of hydrogen bonds and van der Waal contacts (Figure 2B). The crystal structure revealed a closed-state IDE dimer that is nearly identical to those reported previously (Figure 2—figure supplement 1D)(Guo et al., 2010; Malito et al., 2008b2008; Manolopoulou et al., 2009; Ren et al., 2010; Shen et al., 2006). All crystal structures of IDE dimer solved so far are in the closed state, likely due to the constraints imposed by the crystal lattice. This illustrates the challenge in using crystallography to decipher the structure of open-state IDE.

In order to ensure that Fab binding does not alter the conformation and function of IDE, we applied HDX-MS to assess whether Fab_{H11-E} causes noticeable global change in IDE conformations in solution because HDX-MS not only probes the binding regions of a given protein with its partners but also examines protein dynamics and regional stability (Chung et al., 2011; Li et al., 2011; Marciano et al., 2014). As predicted from the Fab_{H11-E}-bound IDE crystal structure, we found epitope residues 374–394 to be the primary region that displays strong reduction in HDX. Two additional regions, residues 297 to 303 and residues 501 to 508, also show moderate reduction in HDX in response to Fab_{H11-E} binding (Figure 2C, Figure 2—figure supplements 2–4). Together, these three regions form a conformational binding epitope, which is in an excellent agreement with our crystal structure. As there is no major change in HDX between IDE alone and Fab_{H11-E}-bound IDE that is distal to Fab_{H11-E} binding site, our HDX-MS data also suggest that Fab_{H11-E} binding has a minimal effect on the conformation dynamics or regional stability of IDE in solution. We only found a minor reduction in HDX in a small region, residues 169 to 198, which is a part of IDE door subdomain that contains the catalytic zinc ion. Interestingly, the stabilization of IDE door subdomain is a key feature induced by substrate binding, which is discussed in details in 'substrate-induced conformational change of IDE'. This could explain a 50% enhancement of IDE catalytic activity upon Fab_{H11-E} binding (Figure 2—figure supplement 1C). Altogether, our data suggests that Fab_{H11-E} does not significantly alter the global structure or activity of IDE. Thus, the cryoEM structures of Fab_{H11-E}-bound IDE is likely to represent the conformations of IDE dimer in solution.

We then performed cryoEM structural analysis of the Fab_{H11-E}-bound IDE dimer in the presence and absence of insulin. 3D maps were reconstructed from 388,643 and 762,283 particles for apo- and insulin-bound IDE-Fab_{H11-E} complex, respectively (Figure 2D–F; Figure 2—figure supplements 5–10; Supplementary file 2–3). A cryoEM map of the insulin-bound IDE-Fab_{H11-E} was constructed using 218,162 particles initially, refined, and solved at 4.1 Å resolution, which confirms how Fab_{H11-E}

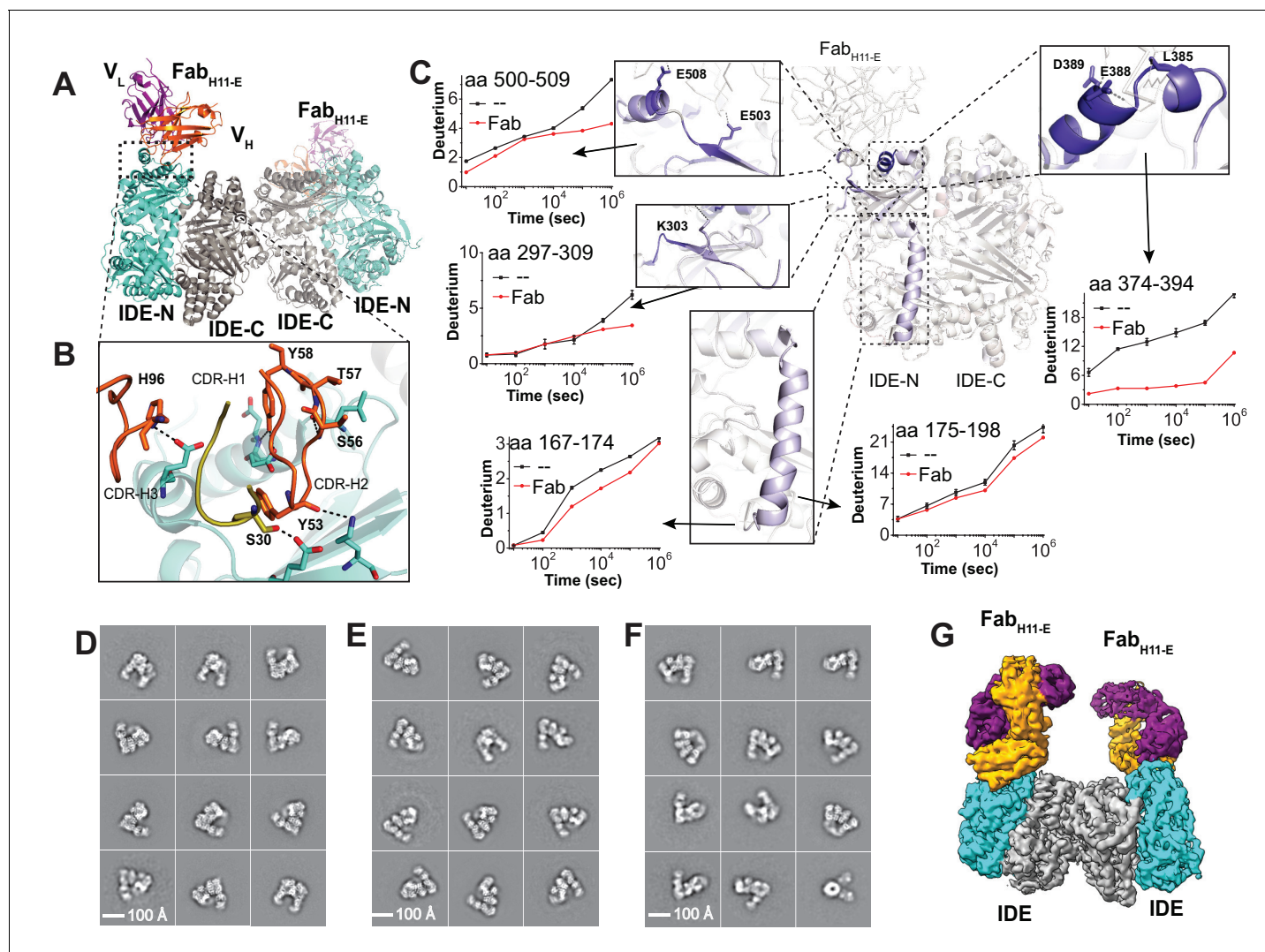


Figure 2. Structures of IDE-Fab_{H11-E}-bound IDE dimer. (A) Overall structure of Fab_{H11-E}-bound IDE dimer in ribbon representation (PDB code: 5UOE). IDE-N and IDE-C are colored in cyan and grey, respectively; The heavy and light chains of Fab_{H11-E} are colored in orange and purple, respectively. (B) Detailed interactions between IDE and Fab_{H11-E}. The key residues involved in the interaction of IDE with Fab_{H11-E} were calculated using PDBePISA (Krissinel and Henrick, 2007). (C) Changes of hydrogen/deuterium exchange of IDE induced by the binding of Fab_{H11-E}. Representative 2D class averages of (D) insulin-bound IDE-Fab_{H11-E}, (E) Apo IDE-Fab_{H11-E}-bound IDE from untilted micrographs and (F) Apo IDE-Fab_{H11-E}-bound IDE from 30 degree titled micrographs. (G) Electron density map of IDE-Fab_{H11-E}-bound IDE dimer in the presence of insulin.

DOI: <https://doi.org/10.7554/eLife.33572.003>

The following figure supplements are available for figure 2:

Figure supplement 1. Characterization of IDE-Fab_{H11-E}.

DOI: <https://doi.org/10.7554/eLife.33572.004>

Figure supplement 2. Pepsin digestion maps of IDE for HDX-MS analysis.

DOI: <https://doi.org/10.7554/eLife.33572.005>

Figure supplement 3. Amide hydrogen-deuterium exchange profiles of IDE alone (A) and IDE in the presence of Fab_{H11-E} (B).

DOI: <https://doi.org/10.7554/eLife.33572.006>

Figure supplement 4. HDX-MS analysis of IDE-Fab_{H11-E} interaction.

DOI: <https://doi.org/10.7554/eLife.33572.007>

Figure supplement 5. Cryo-electron micrographs and 2D class averages of insulin-bound IDE-Fab_{H11-E}.

DOI: <https://doi.org/10.7554/eLife.33572.008>

Figure supplement 6. Cryo-electron micrographs and 2D class averages of untilted Apo IDE-Fab_{H11-E}.

DOI: <https://doi.org/10.7554/eLife.33572.009>

Figure supplement 7. Cryo-electron micrographs and 2D class averages of tilted Apo IDE-Fab_{H11-E}.

Figure 2 continued on next page

Figure 2 continued

DOI: <https://doi.org/10.7554/eLife.33572.010>

Figure supplement 8. Flow chart of cryoEM data processing.

DOI: <https://doi.org/10.7554/eLife.33572.011>

Figure supplement 9. CryoEM statistics of apo IDE-Fab_{H11-E} and insulin-bound IDE-Fab_{H11-E}.

DOI: <https://doi.org/10.7554/eLife.33572.012>

Figure supplement 10. Overall fit of cryoEM density map to the structure models.

DOI: <https://doi.org/10.7554/eLife.33572.013>

binds IDE (**Figure 2G**, **Figure 2—figure supplement 8B**, **Supplementary file 3**). We further improved the resolution of the IDE dimer using IDE dimer-focused classification with signal subtraction and refinement, resulting in a map and structural model with an overall resolution of 3.7 Å (**Figure 2—figure supplements 8B**, **9** and **10**, **Supplementary file 3**). Apo Fab_{H11-E}-bound IDE showed a highly preferred orientation in vitreous ice. Thus, images were acquired with the grid tilted at an angle to the electron beam, which allowed better sampling of other orientations (**Figure 2F**, **Figure 2—figure supplement 9B**) (*Tan et al., 2017*). The initial 3D refinement of apo IDE-Fab_{H11-E} of 151,868 particles had a resolution of 4.4 Å. Further 3D classification revealed three major conformations and structural models were built (**Supplementary file 3**). We again applied IDE dimer-focused classification with signal subtraction of the IDE-Fab_{H11-E} dimer to refine each conformation separately, which improved the resolution significantly (**Figure 2—figure supplement 9A**, **Supplementary file 3**). The three apo-IDE structures derive from combinations of the IDE partial open (pO) and open (O) states (**Figure 3A**). The dimer with one open and one partially open conformational subunit (open/partial open, 110,499 particles) reached an overall resolution of 4.2 Å (**Figure 3A**, **Figure 2—figure supplements 5–9**, **Supplementary file 3**). The dimer with two open conformational subunits (open/open, 24,425 particles) resulted in an overall resolution of 6.5 Å (**Figure 3A**, **Figure 2—figure supplements 5–9**, **Supplementary file 3**). The dimer with two partially open conformational subunits (partial open/partial open, 16,944 particles) reached 6.9 Å resolution (**Figure 3A**, **Figure 2—figure supplements 5–9**, **Supplementary file 3**).

CryoEM structures of IDE dimer

CryoEM analysis reveals four novel IDE dimer structures, one from insulin-bound IDE and three from apo-IDE (**Figure 3A**). The cryoEM structure of the insulin-bound IDE dimer at 3.7 Å resolution (**Videos 1–2**) shows that both IDE subunits adopt a similar but not identical partially closed (pC) state that differs from the previously reported closed-state IDE (**Figure 3B**, **Figure 3—figure supplement 1**, **Supplementary file 4**) (*Guo et al., 2010*; *Malito et al., 2008b2008*; *Manolopoulou et al., 2009*; *Ren et al., 2010*; *Shen et al., 2006*). The buried surface area between IDE-N and IDE-C and distance between center of mass (COM) of D1 and D4 in the cryoEM pC state is nearly identical to those in the closed-state IDE shown by X-ray crystallographic studies (**Figure 3B**, **Supplementary file 4**). However, this pC state has an approximately 2° decreased dihedral angle between the COM of four homologous domains, D1-D4, compared to those in the closed-state IDE (**Figure 3B**, **Supplementary file 4**), suggesting a potential gliding motion allows IDE to shift between partially closed and closed states. The position of insulin in the catalytic cleft of the cryoEM maps reveals that the IDE pC state is ready for catalysis. Thus, both IDE pC and C states are catalytically competent.

The combinations of the IDE partial open (pO) and open (O) states results in three apo-IDE structures (**Figure 3A**). The IDE pO and O states differs from the pC and C states by 5 Å to 24 Å increases in the distance between D1 and D4 and 7° to 17° increases in the dihedral angle, respectively (**Figure 3B**, **Figure 3—figure supplement 1**, **Supplementary file 4**, **Video 1**). These changes result in decreased buried surface between IDE-N and IDE-C in pO and O states. The three conformers have resolution limits which correlated well with their relative populations: O/pO (4.2 Å, 73%), O/O (6.5 Å, 16%), and pO/pO (6.9 Å, 11%). Interestingly, the conformation of pO and O states in the pO/O IDE dimer differ significantly from those in pO/pO or O/O IDE dimer. Furthermore, two subunits within O/O or pO/pO states have noticeable differences in the distance and buried surface between IDE-N and IDE-C and the dihedral angle (**Supplementary file 4**). Such differences provide a potential explanation for the mechanism by which dimerization-induced allostery regulates the

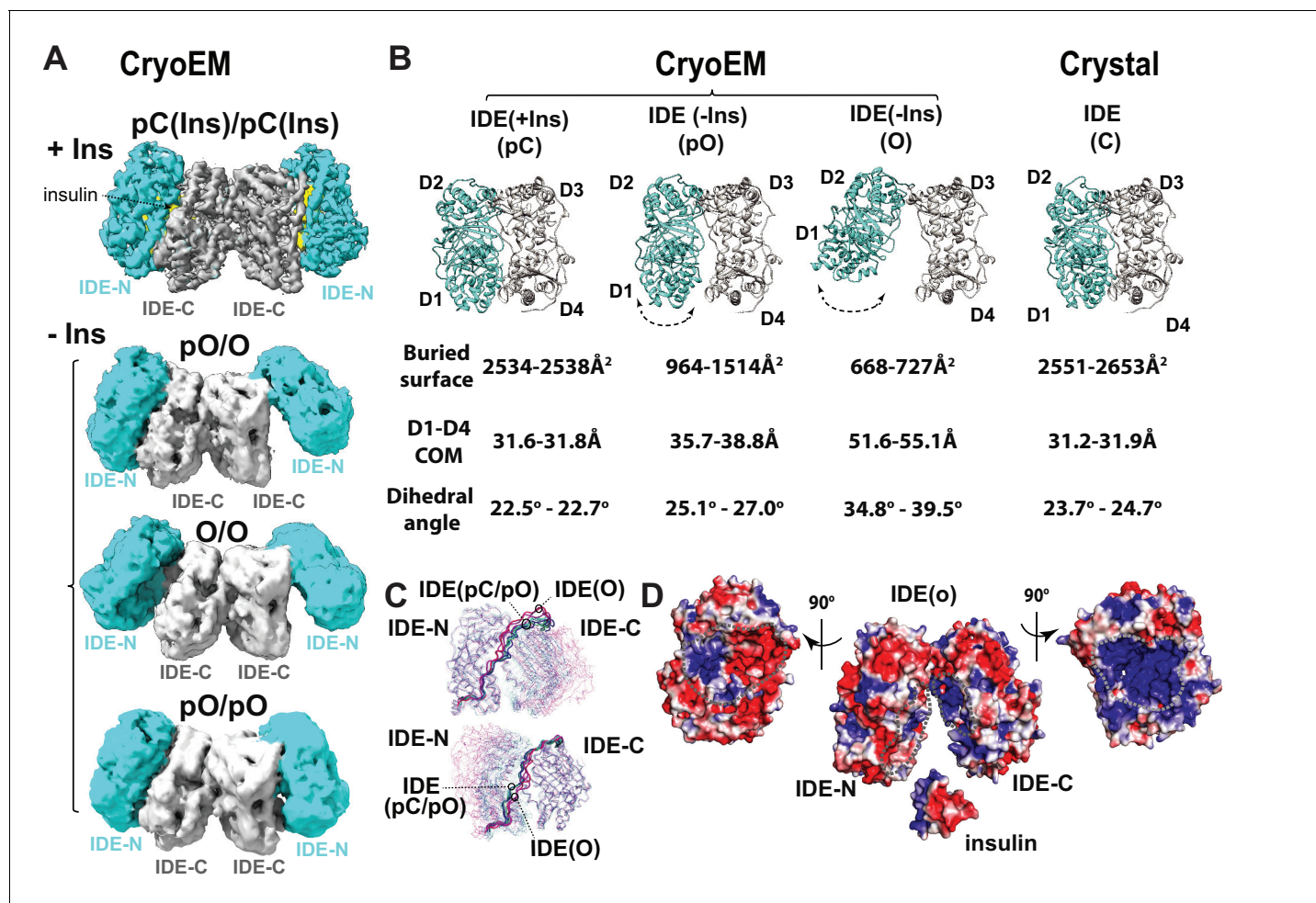


Figure 3. CryoEM IDE dimer. (A) Overall structures of IDE dimer in the presence and absence of insulin. Models are shown as ribbons within the electron density map. O, open state; pO, partially open state; pC, partially-closed state. IDE-N and IDE-C are colored in cyan and grey, respectively; insulin inside the catalytic chamber of IDE is colored in yellow. For simplicity, Fab is not shown. (B) Comparison of four distinct conformational states within IDE structures; two pC states in the insulin-bound cryoEM IDE structure, three pO and three O states in apo-IDE cryoEM structures, and a closed structure from previous crystallographic work (Guo et al., 2010; Malito et al., 2008b2008; Manolopoulou et al., 2009; Noinaj et al., 2011; Ren et al., 2010; Shen et al., 2006). The buried surface between IDE-N and IDE-C, distance between the center of mass (COM) of IDE D1 and D4 domains, and dihedral angles (absolute values) between COM of IDE D1-D2 and COM of D3-D4 are shown below the ribbon presentation of IDE structures. (C) Structural comparison of IDE states aligned by IDE-N (top) or IDE-C (bottom), showing rigid body motion of IDE-N and IDE-C guided by the loop connecting IDE-N and IDE-C. (D) Structural basis of IDE open structure primed to capture insulin by size and charge complementarity. The boundaries for the substrate-binding catalytic chambers of IDE-N and IDE-C are marked by a dashed line. The color scale is set from -3 kT/e (red) to 3 kT/e (blue) calculated using APBS 2.1.

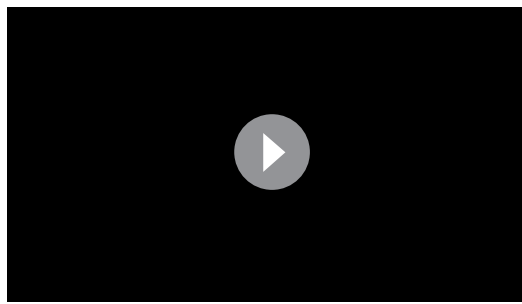
DOI: <https://doi.org/10.7554/eLife.33572.014>

The following figure supplement is available for figure 3:

Figure supplement 1. Comparison of four distinct conformers of IDE, Open (O), partially open (pO), partially closed (pC), and closed (C).

DOI: <https://doi.org/10.7554/eLife.33572.015>

catalytic activity of IDE (Figure 3B, Figure 3—figure supplement 1) (McCord et al., 2013; Ralat et al., 2011; Song et al., 2010). Open-state IDE has an opening just wide enough to capture its substrates, for example, insulin, TGF- α , and MIP-1 α/β , allowing the IDE catalytic chamber to attract these substrates with high dipole moment via charge complementarity (Figure 3D) (Guo et al., 2010; Manolopoulou et al., 2009; Ren et al., 2010).



Video 1. Overall fit of human dimeric IDE structures with the electron density maps. Scheme 1: CryoEM structure of human insulin-bound dimeric IDE at 3.8 angstrom resolution. Electron density map colored in grey, IDE colored in cyan and in the ribbon representation, and insulin colored in yellow. Scheme 2: Cryo EM structure of human apo-IDE at 4.1 angstrom resolution that has one subunit in the partially-open state and the other in the open state. Electron density map in grey and IDE colored in pale green and in ribbon representation. This is the dominant conformational state of apo-IDE. Scheme 3: Cryo EM structure of human apo-IDE at 5.5 angstrom resolution that has both subunits in the open state. Electron density map in grey and IDE colored in magenta and in ribbon representation. Scheme 4: Cryo EM structure of human apo-IDE at 5.9 angstrom resolution that has both subunits in the partially-open state. Electron density map in grey and IDE colored in purple and in ribbon representation.

DOI: <https://doi.org/10.7554/eLife.33572.016>

analysis to obtain rate constants for the insulin-induced open-closed transition of IDE. Time-resolved SAXS experiments were done using a microfluidic laminar flow mixer adapted from the design initially developed for time resolved fluorescence studies (Park *et al.*, 2008; Park *et al.*, 2006). We found that the change in R_g value caused by the rapid mixing of IDE with insulin fit well with a single exponential decay with $\tau = 0.1$ s (Figure 4B). Thus, the timeframe required for insulin to induce conformational switching from a high R_g state to a low R_g state is close to the rate of degradation of insulin by IDE (~ 2 s⁻¹). This suggests that insulin-induced IDE open-closed transition is likely a key rate-limiting step for insulin clearance by IDE.

Substrate-induced conformational changes of IDE

In a previous crystal structure of the Fab1-bound closed apo-IDE, one subunit within the IDE dimer did not have the electron density for the IDE door subdomain (McCord *et al.*, 2013). This leads to the hypothesis that IDE has a catalytic zinc-containing door subdomain that is partially unfolded and/or undergoes a rigid body motion. This hypothesis predicts that, under the crystallization conditions used for Fab1-bound closed apo-IDE crystal structure, the presence of IDE substrates would stabilize IDE door domain, rendering it visible. We thus solved crystal structures for Fab1-bound IDE structures in the presence of A β and insulin at 3.5 Å and 3.9 Å resolution, respectively ($R/R_{\text{free}} = 23/27\%$, $R/\text{free} = 24/29\%$) and Fab1_E- and insulin-bound IDE at 3.3 Å resolution ($R/R_{\text{free}} = 20/25\%$) (Supplementary file 1). Instead of being absent, as in the apo-IDE crystal structure (McCord *et al.*, 2013), we found that the door subdomain of IDE is clearly visible in these structures (Figure 5A). In fact, these IDE structures are nearly identical to closed-state IDE determined in the previously reported insulin- or A β -bound IDE (RMSD = 0.46 and 0.56 Å, respectively, Figure 5—figure supplement 1). Consistent with that notion that this is induced by substrate, unfolded A β or insulin is

SAXS analysis of IDE

Our cryoEM structures reveal that only open-state IDE can capture its prototypical substrate, insulin, and release cleaved products. The interaction of open-state IDE with insulin likely facilitates the open-closed transition of IDE. We chose SAXS to test this hypothesis because SAXS provides the ensemble information regarding size and shape of molecules in solution (Blanchet and Svergun, 2013). To exclude IDE monomer and larger aggregates, we used size exclusion chromatography in-line with SAXS. Such a SAXS profile of the IDE dimer allows us to assess the distribution of open- and closed-state IDE in the presence and absence of insulin with better precision. We evaluated the experimental data with the prediction from our cryoEM models using the radius of gyration (R_g), the average of square center of mass distances of the molecule, and the distance distribution function, $p(r)$ (Figure 4A, Figure 4—figure supplement 1). Our SAXS data showed that IDE in solution exist in equilibrium between open and partially open states and that insulin constrained the IDE dimer into mostly partially closed or closed states. This agrees with our observation in cryoEM.

Enzyme kinetic analysis estimated that insulin degradation by IDE occurs reasonably rapidly, up to ~ 2 per second (Manolopoulou *et al.*, 2009). To assess whether the insulin-induced open-closed transition of IDE could limit insulin degradation by IDE, we used time-resolved SAXS anal-

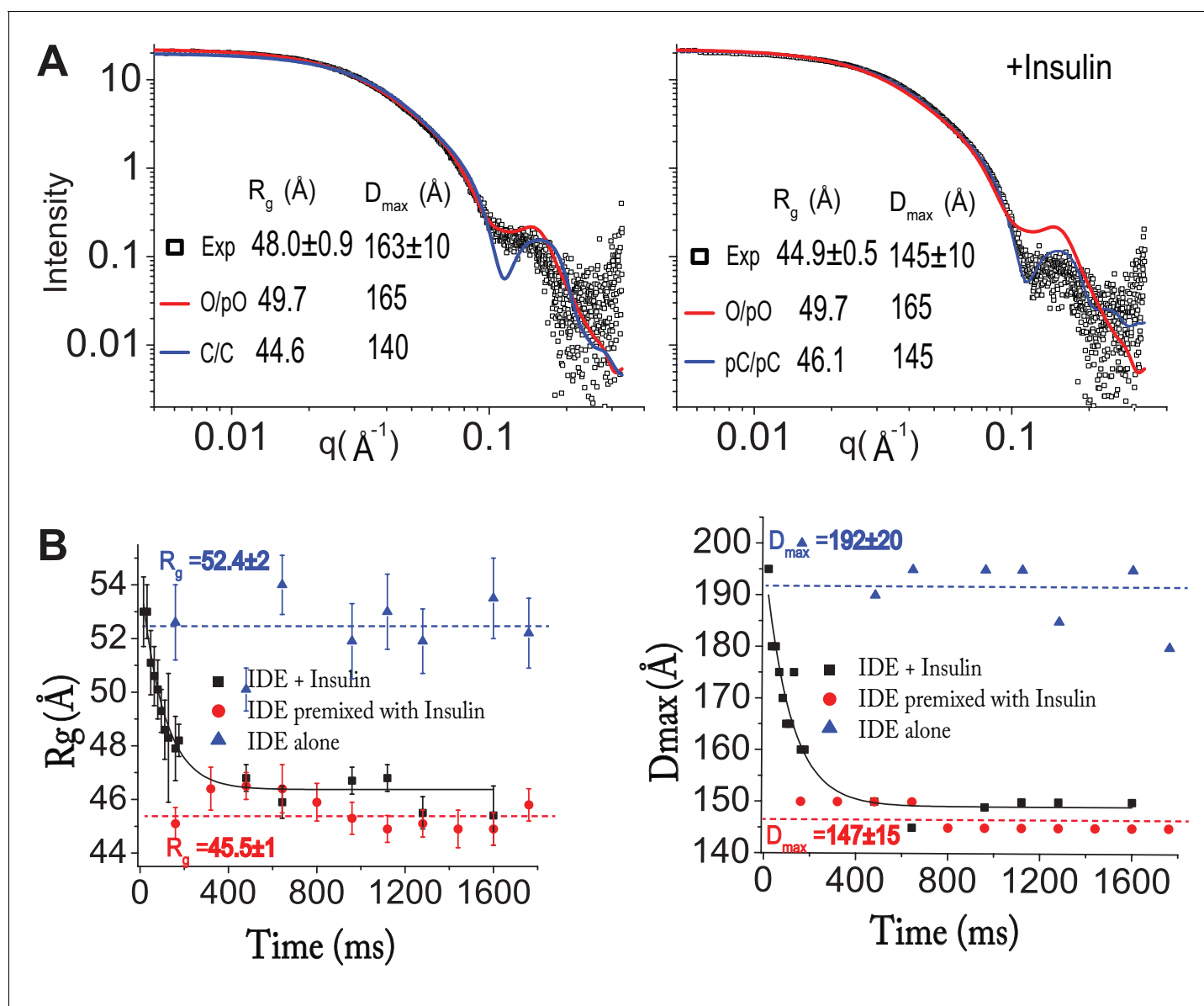


Figure 4. Insulin-induced conformational changes of IDE revealed by SAXS. (A) Scattering curves from SEC-SAXS analysis using 2–3 mg IDE in the presence (left) or absence (right) of fourfold molar excess of insulin. Solid red and blue lines represent the predicted SAXS curves based on indicated IDE structures. (B) Time-resolved SAXS analysis of IDE-insulin interaction. Rapid mixing of IDE with insulin resulted in time-dependent reduction of R_g with $\tau = 0.1$ s.

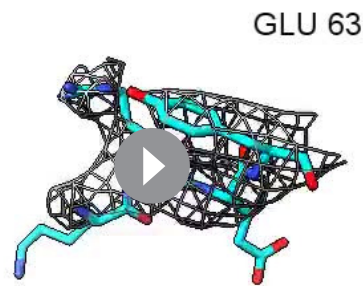
DOI: <https://doi.org/10.7554/eLife.33572.018>

The following figure supplement is available for figure 4:

Figure supplement 1. SAXS analysis of IDE.

DOI: <https://doi.org/10.7554/eLife.33572.019>

clearly visible inside the IDE catalytic chamber. This hypothesis also predicts that the IDE door subdomains in the cryoEM structures of apo-IDE dimer would have the higher thermal B factors than those in that of insulin-bound IDE dimer. Indeed, while clearly visible, the IDE door subdomain, particularly the catalytic zinc-coordinating $\alpha 4$ helix, has significantly higher thermal B factors than in the insulin-bound structure (Figure 5B, Figure 5—figure supplement 2). The presence of insulin thus profoundly reduces the thermal B factors of IDE door subdomain (Figure 5B, Figure 5—figure supplement 2). Together, our data support the stabilization of the partial unfolding and/or motion of



Video 2. Fit of individual residues of an IDE subunit of insulin-bound IDE at 3.8 angstrom resolution with the electron density map. The movie is 30 minutes long and is designed for the viewer to zip through residues by the control bar of the movie running software.

DOI: <https://doi.org/10.7554/eLife.33572.017>

BDM44768 and 6bK directly bind, both inhibitors also decreased HDX in the IDE door subdomain (**Figure 5C and D, Figure 5—figure supplements 3–6**). These data support the dynamic nature of the catalytic cleft within IDE door subdomain and the importance of this region to the proper functioning of the enzyme.

The combination of HDX-MS with cryoEM structures offers a framework for studying the detailed conformational changes of IDE induced by its substrates. Multiple regions in IDE exhibited a significant reduction in HDX upon insulin binding (**Figure 6A, Figure 6—figure supplements 1–4**). These regions correlate well with those that have higher thermal B factors in our cryoEM structures when insulin is absent (**Figure 5B**). These include known substrate-binding sites of IDE: the door subdomain that contains the zinc catalytic site in domain D1, exosite in domain D2 that anchors the N-terminal region of IDE substrates, and residues 821–830 in domain D4 that binds the P1' and P2' residues of IDE substrates after the scissile bond (**McCord et al., 2013; Shen et al., 2006**). Insulin also reduced HDX in regions that directly bind IDE door subdomain including the hydrophobic rich H loop, residues 668–673 and residues 821–830 (**McCord et al., 2013**). Together, these data support the conclusion that the binding of substrate stabilizes the IDE catalytic site. Furthermore, insulin binding also reduced the HDX at the IDE-N and IDE-C joining loop and its underlying α -helices, α 11 and α 20, which is consistent with our SAXS data showing that insulin facilitates the open-closed transition of IDE. A similar pattern of HDX reduction in IDE was also observed when IDE was mixed with $A\beta_{1-40}$ (**Figure 6B**). However, subtle but noticeable differences exist that could aid the search to achieve substrate-selective modulation of IDE. For example, insulin stabilizes the entire IDE door subdomain (residues 170–237) while $A\beta$ only stabilizes the zinc-binding portion of IDE door subdomain (residues 170–203) (**Figure 6—figure supplements 3–4**). Together, our data indicate that the binding of substrates promotes the open to closed transition of IDE and stabilizes the IDE catalytic site for substrate-assisted catalysis.

Mechanism for the processive degradation of insulin by IDE

IDE processively cuts insulin into two pieces without breaking the disulfide bonds that hold the insulin A and B chains together (**Figure 7A**) (**Manolopoulou et al., 2009**). However, previously reported insulin-bound IDE structures could not explain the processivity of insulin degradation by IDE (**Manolopoulou et al., 2009**). In our cryoEM and crystal structures of insulin-bound IDE, extra electron density was clearly visible inside the IDE catalytic chamber (**Figure 7B and C, Figure 7—figure supplement 1**), and the insulin structure is quite different to that reported previously (**Manolopoulou et al., 2009**). The extra density fit well with regions of an unfolded insulin A or B chain with a known scissile bond properly residing at the IDE catalytic site (**Figure 7A and B, Figure 7—figure supplement 2**). Additional density is present for part of the other insulin chain, linked by the expected intermolecular disulfide bonds (**Figure 7A, Figure 7—figure supplement 2**). We

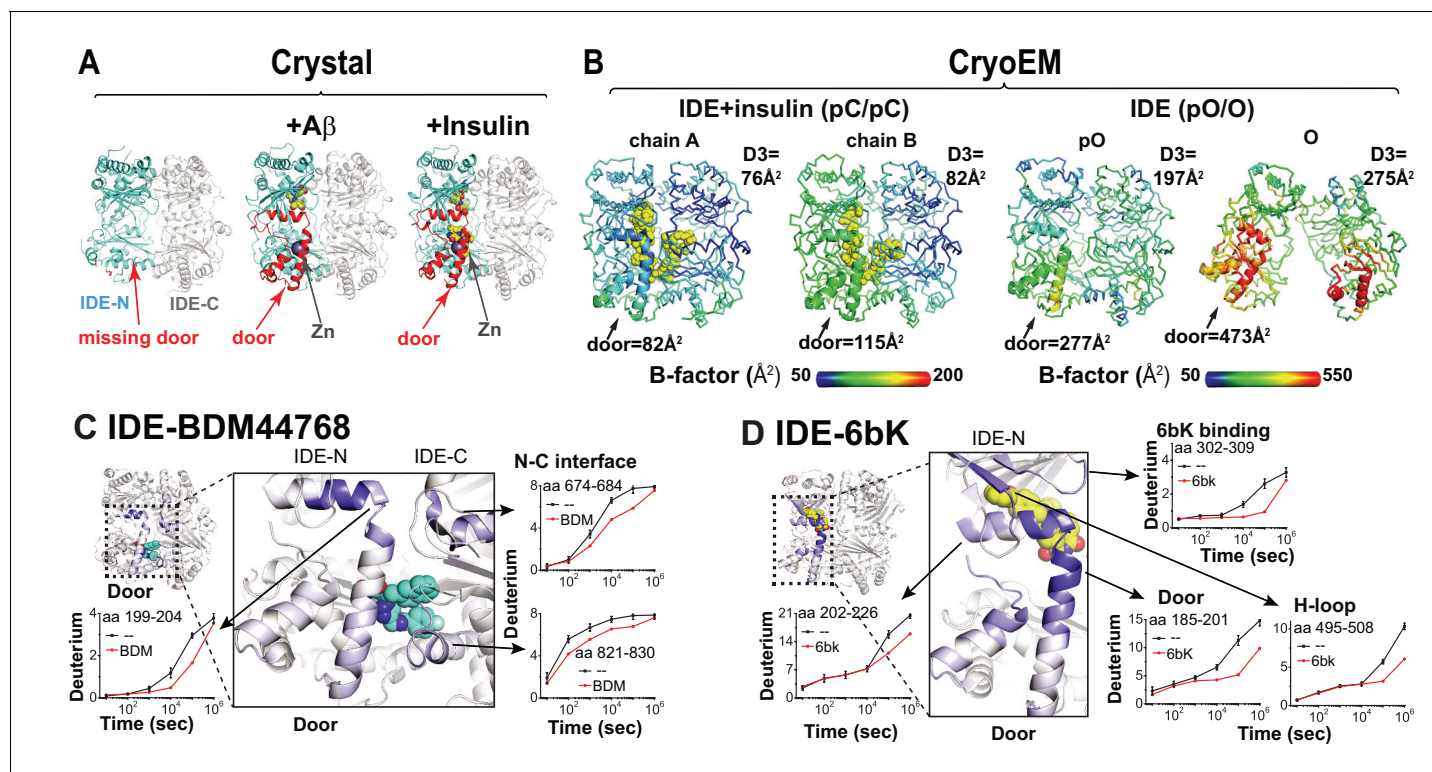


Figure 5. Conformational dynamics of IDE door domain. (A) Comparison of crystal structures of Fab1-bound IDE alone (PDB code: 4IDF), Fab1- and A β -bound IDE (PDB code: 4MIC) and Fab1- and insulin-bound IDE (PDB code: 5WOB). For simplicity, only the subunit of the dimeric IDE that has the profound change in IDE door subdomain is shown and Fab1 is not shown. (B) Thermal B factors of two IDE subunits within cryoEM IDE dimer structures of insulin-bound pC/pC state IDE (PDB code: 6B3Q) and pO/O apo-state IDE (PDB code: 6BF8). Averaged B factors of IDE door and D3 are shown for comparison. For simplicity, Fab_{H11-E} is not shown. (C, D) Changes in H/D exchange of IDE induced by inhibitors, BDM44768 and 6bK. The changes in H/D are mapped and the progress curve of regions with significant changes are shown.

DOI: <https://doi.org/10.7554/eLife.33572.020>

The following figure supplements are available for figure 5:

Figure supplement 1. Comparison of crystal structures of insulin- or A β -bound IDE.

DOI: <https://doi.org/10.7554/eLife.33572.021>

Figure supplement 2. Comparison of thermal B factor distribution of four cryoEM IDE structures, and two crystal structures.

DOI: <https://doi.org/10.7554/eLife.33572.022>

Figure supplement 3. Amide hydrogen-deuterium exchange profiles of IDE alone (A) and IDE in the presence of BDM44768 (B).

DOI: <https://doi.org/10.7554/eLife.33572.023>

Figure supplement 4. Amide hydrogen-deuterium exchange profiles of IDE alone (A) and IDE in the presence of 6bK (B).

DOI: <https://doi.org/10.7554/eLife.33572.024>

Figure supplement 5. HDX-MS analysis of IDE-small molecule inhibitor interaction.

DOI: <https://doi.org/10.7554/eLife.33572.025>

Figure supplement 6. Progression curves that have the significant difference in HDX of IDE when 6bK or BDM-44768 (BDM) were present.

DOI: <https://doi.org/10.7554/eLife.33572.026>

also found that the N-terminus displays density characteristic of phenylalanine 1 of the insulin B chain, while other density corresponds to the ring structure formed by an intramolecular disulfide and a bulky tyrosine 14 side chain at the P1' cleavage site, which are characteristic of the insulin A chain (Figure 7—figure supplement 2). Thus, this density has key features that can be contributed by either chain and can be best interpreted as an ensemble of unfolded insulin A and B chains, not belonging solely to either chain.

Together, these structures provide the molecular basis of how IDE could processively cut insulin into two pieces without having to choose which insulin chain to cut first. Upon insulin capture by IDE catalytic chamber, IDE stochastically cuts whichever of either insulin A or B chain binds the IDE catalytic cleft first after insulin unfolding inside the catalytic chamber (Figure 8A). Our structures also

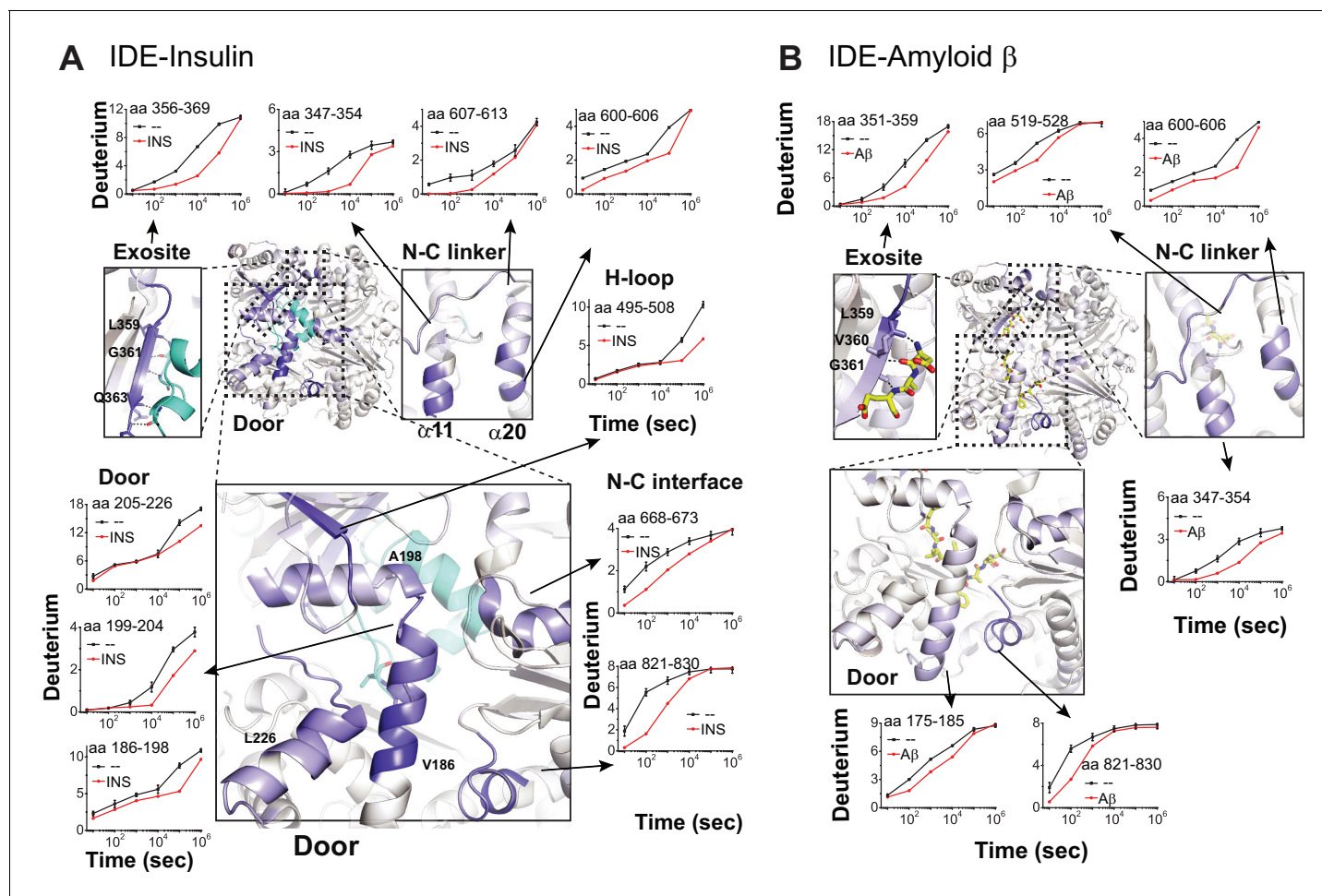


Figure 6. Substrate-induced changes in H/D exchange of IDE. (A) Major changes in H/D exchange of IDE induced by insulin. Changes in H/D are mapped onto IDE structure and the progress curve of regions with significant changes are shown. (B) Major changes in H/D exchange of IDE induced by A β .

DOI: <https://doi.org/10.7554/eLife.33572.027>

The following figure supplements are available for figure 6:

Figure supplement 1. Amide hydrogen-deuterium exchange profiles of IDE alone (A) and IDE in the presence of insulin (B).

DOI: <https://doi.org/10.7554/eLife.33572.028>

Figure supplement 2. Amide hydrogen-deuterium exchange profiles of IDE alone (A) and IDE in the presence of A β (B).

DOI: <https://doi.org/10.7554/eLife.33572.029>

Figure supplement 3. HDX-MS analysis of IDE-substrate interaction.

DOI: <https://doi.org/10.7554/eLife.33572.030>

Figure supplement 4. Progression curves that have the significant difference in HDX of IDE when insulin (INS) or A β were present.

DOI: <https://doi.org/10.7554/eLife.33572.031>

reveal that the N-terminus of insulin interacts extensively with the IDE-N exosite while IDE-C makes substantial contacts with the C-terminal part of insulin. As the N- and C-terminal parts of insulin of the singly-cut insulin are still joined by the inter-molecular disulfide bond, insulin could still effectively keep IDE in the closed conformation. The subsequent unfolding of cleaved insulin leads to processive cleavage of the other insulin chain (**Figure 8A**). The resulting N- and C-terminal insulin fragments would then be released upon the closed to open transition of IDE.

Discussion

By combining cryoEM, crystallography, SAXS, and HDX-MS, our integrative structural analysis reveals the molecular details of how IDE undergoes open to closed conformational switches for the capture, unfolding, and degradation of insulin and peptides that tend to form amyloid fibrils (**Figure 8B**). By rigid-body motion between IDE-N and IDE-C, IDE switches between O and pO states. This results in three possible conformers where the O/pO dimer is dominant (**Figure 8B, Video 3**). Only open-state IDE captures large peptide substrates (e.g. insulin and A β). The degree of opening and the charge distribution of the IDE catalytic chamber determine which peptides are captured by IDE depending on their size and high dipole moment (**Figure 3D**). The motions between open- and closed-state IDE, in conjunction with the selective interactions of the IDE catalytic chamber with these peptides, for example, IDE exosite with peptide's N-terminus, creates a force to selectively unfold amyloidogenic peptides. The exposed β -strand of these peptides then stabilizes the inherently unstable IDE catalytic center, leading to the degradation of amyloidogenic peptides by IDE.

The cryoEM structures of open-state IDE suggest the additional ways how IDE may work. Based on the size of catalytic chamber in the closed-state IDE, it is postulated that the entrapment of substrates inside the enclosed catalytic chamber of IDE is required for catalysis (**Malito et al., 2008a; Shen et al., 2006**). Thus, IDE only degrades peptides that are capable of fitting into the IDE catalytic chamber. This explains well why all of well-characterized IDE substrates are peptides less than 80 amino acids long (**Malito et al., 2008a; Tang, 2016**). This model has successfully guided the identification of CCL3 and CCL4 as novel IDE substrates and the combination of the oligomerization of these chemokines and their degradation by IDE modulates the effectiveness of the chemotactic gradient formed by these chemokines (**Ren et al., 2010**). It does not escape our attention that IDE should be able to degrade larger proteins if such proteins are readily captured by open-state IDE via the charge and surface complementarity and can effectively stabilize IDE catalytic cleft. We also envision that open-state IDE can bind α -synuclein oligomers and alter the kinetics of oligomerization process, which explains how IDE reduces the amyloid fibril formation of α -synuclein in vitro (**Sharma et al., 2015**).

The catalytic activity of IDE is allosterically regulated by its substrate, ATP, and other partner proteins (**McCord et al., 2013; Ralat et al., 2011; Song et al., 2003; Song et al., 2010; Tang, 2016**). Based on our data, we put forth a model to explain how the equilibrium between IDE open and 'closed' states facilitates IDE allostery (for simplicity, we group structurally similar pO, pC, and C states into the 'closed' state that is distinct from open-state IDE). By the extensive contacts between IDE-C domains, IDE readily dimerizes ($K_d \approx 10$ nM) (**Li et al., 2006; Shen et al., 2006**). Our cryoEM data reveal that two IDE-N domains within the IDE dimer undergoes rigid body motion, allowing IDE to undergo the transition between the open and 'closed' states without the assistance of substrate (**Figure 8B**). Furthermore, the preferred O/pO combination indicates that the motion of IDE-N in one subunit of IDE dimer is not independent from the other (**Figure 8B**). We thus envision that the preferred combination of the open and 'closed' states within the IDE dimer would allow the substrate-induced closure of one subunit to promote the switch of the other subunit to the open state, allowing cleaved products to be released or substrate captured (**Video 3** synchronized motion 1). Conversely, the opening of one subunit from the 'closed'-state will promote the closure of the other for substrate unfolding and catalysis (**Video 3** synchronized motion 1). Such motions can explain how substrate allosterically regulates IDE activity and how monomerization mutations render IDE less active as well as the lose the ATP- and substrate-mediated regulation (**Ralat et al., 2011; Song et al., 2003; Song et al., 2010**). This model is also consistent with the kinetic studies which show that phenylalanine 530 mutation to alanine at the linker joining IDE-N and IDE-C makes IDE hyperactive and alters allosteric regulation (**McCord et al., 2013**). Our HDX-MS data reveal that the binding of IDE substrate or inhibitor only affects the deuterium exchange at the IDE-N and IDE interface and the linker between IDE-N and IDE-C, not between the interface of two IDE subunits (**Figures 5 and 6**). Thus, our data does not offer an obvious path for substrate-facilitated allosteric communication between IDE subunits. We speculate that IDE allostery is mediated by the collective motions of many atoms in IDE, not by a subset of atoms within a defined path. The detailed mechanism for IDE allostery awaits future MD simulation studies.

Many, if not most, molecular machines are conformationally heterogeneous, adopting a variety of different structural conformers in solution as they adapt form to serve function. CryoEM is uniquely

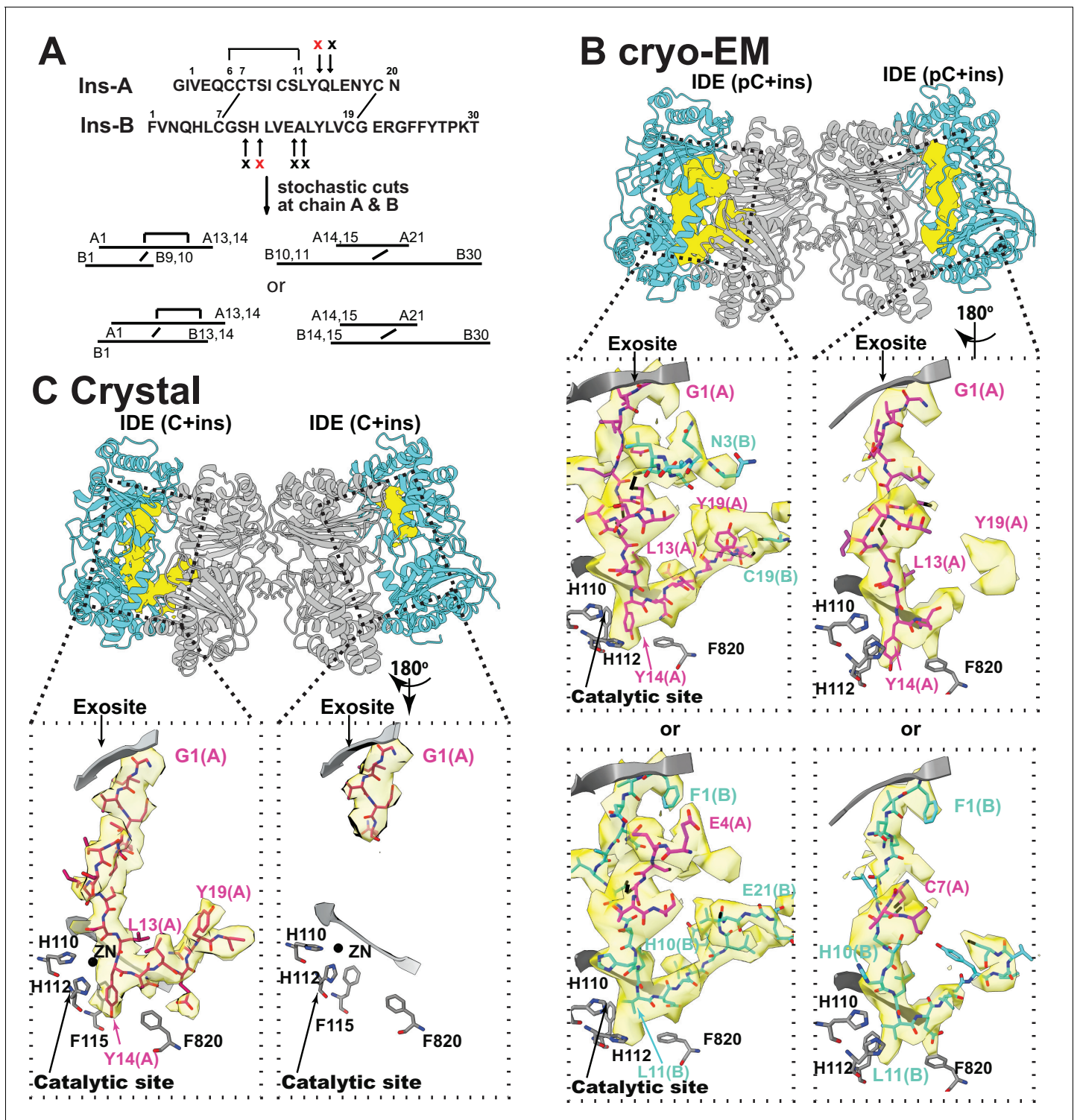


Figure 7. The interaction of IDE with insulin. (A) Cleavage sites of insulin by IDE. The initial cleavages and resulting fragments are shown. The red X marks the scissile bond revealed by insulin-bound IDE structures. (B) CryoEM structure of unfolded insulin inside IDE. The fitting of electron density at the catalytic sites with either insulin A (PDB code: 6B3Q) or B chain (PDB code: 6BFC) are shown. For simplicity, Fab_{H11-E} is not shown. (C) Structure of unfolded insulin inside IDE from insulin bound IDE-Fab1 complex (PDB code: 5WOB). For simplicity, only the fitting of insulin A chain is shown.

DOI: <https://doi.org/10.7554/eLife.33572.032>

The following figure supplements are available for figure 7:

Figure supplement 1. Insulin binding at IDE catalytic chamber from Fab1- and insulin-bound IDE crystal structure at 3.95 Å resolution.

Figure 7 continued on next page

Figure 7 continued

DOI: <https://doi.org/10.7554/eLife.33572.033>**Figure supplement 2.** The fit of the unfolded insulin A or B chain with electron density inside the catalytic chamber of IDE from cryoEM structure of insulin-bound IDE.DOI: <https://doi.org/10.7554/eLife.33572.034>

capable of solving the structures of these large flexible macro-molecules. Improvements in the hardware technology over the past 5 years (Li *et al.*, 2013) now provide for excellent quality images and improvements in software allow for classification of particles of different conformations from a heterogeneous mixture of structures (Scheres, 2012). Our approach to obtain cryoEM structure of the open-state IDE, a key functional state recalcitrant to crystallization, is generally applicable to other proteins. In addition to its relatively small size (220 kDa), the IDE dimer adopts multiple conformational states to fulfill its function. To solve the challenge posed by size and pseudo two-fold symmetry in our system, we included high-affinity IDE-binding Fabs, which increases the size of the complex, breaks the apparent symmetry, and provides excellent fiducials for validating the morphology and resolution of the overall structure. We take advantage of two other technological developments to improve cryoEM structure determination of the IDE dimer. A new vitrification device, Spotiton, allows us to prepare samples embedded in a very thin and even layer of vitrified ice, which improves data quality (Dandey *et al.*, 2018; Razinkov *et al.*, 2016). We also addressed the issues of preferred orientation, quite common for many samples, by acquiring images from gold-coated grids tilted relative to the electron beam (Russo and Passmore, 2014; Tan *et al.*, 2017). In conjunction with the state-of-art hardware and software in data acquisition, these implementations allowed us to obtain near atomic resolution 3D structures of the open-state IDE despite its conformational heterogeneity.

The accumulation of toxic amyloid fibrils is associated with many human diseases and IDE plays a key role in preventing amyloid fibril formation by its proteolytic activities (Jucker and Walker, 2013; Tang, 2016). Accumulating data also suggest that IDE plays non-proteolytic roles to regulate other proteostatic processes, for example, regulating proteasome activity and preventing amyloid fibril formation of α -synuclein (Tang, 2016). As IDE modulates proteostasis by targeting diverse proteins, substrate selective modulation of IDE activity is crucial to realize IDE-based therapy (Pivovarova *et al.*, 2016; Tang, 2016). Indeed, noticeable differences in the reduction of HDX between insulin- and A β -bound IDE exist (Figure 6A and B). Together with our cryoEM structures, our studies offer a road map to develop insulin-selective inhibitors or A β -selective enhancers to treat diabetes and Alzheimer's disease.

Materials and methods

Key resources table

Reagent type (species) or resource	Designation	Source or reference	Identifiers	Additional information
Antibody	Synthetic anti-IDE antibody Fab fragment (Fab _{H11-E})	This study	NA	About 5 mg/ml for crystallization, and 0.15 mg/ml for cryoEM.
Antibody	Synthetic anti-IDE antibody Fab fragment Fab1Fab1	(McCord <i>et al.</i> , 2013)	NA	About 5 mg/ml for crystallization.
Recombinant protein (Human)	Cysteine-free IDE	This study	NA	Described as above.
Recombinant protein (Human)	Cysteine-free IDE-E111Q	This study	NA	Described as above.
Recombinant protein (Human)	Insulin	Sigma-Aldrich	234-279-7	
Recombinant protein (Human)	Amyloid β	(King <i>et al.</i> , 2014)	NA	

Continued on next page

Continued

Reagent type (species) or resource	Designation	Source or reference	Identifiers	Additional information
Recombinant protein (Human)	Pepsin	Sigma-Aldrich	P6887-1G	
Chemical compound, drug	BDM44768	(<i>Deprez-Poulain et al., 2015a</i>)	NA	
Chemical compound, drug	6bK	(<i>Maianti et al., 2014</i>)	NA	
Chemical compound	D2O	Cambridge Isotope Laboratories, Inc.	DLM-4-1L	
Software, algorithm	Leginon 3.3	(<i>Suloway et al., 2005</i>)	NA	http://emg.nysbc.org/redmine/projects/legion/wiki/Leginon_Homepage
Software, algorithm	DoGpicker	(<i>Voss et al., 2009</i>)	NA	http://emg.nysbc.org/redmine/projects/software/wiki/DoGpicker
Software, algorithm	MotionCor2	(<i>Zheng et al., 2017</i>)	NA	http://msg.ucsf.edu/em/software/motioncor2.html
Software, algorithm	Relion2.0	(<i>Scheres, 2012</i>)	NA	http://www2.mrc-lmb.cam.ac.uk/relion/index.php/Main_Page
Software, algorithm	Relion2.1	(<i>Scheres, 2012</i>)	NA	http://www2.mrc-lmb.cam.ac.uk/relion/index.php/Main_Page
Software, algorithm	3DFSC	(<i>Tan et al., 2017</i>)	NA	https://github.com/nysbc/Anisotropy
Software, algorithm	UCSF ChimeraX	(<i>Goddard et al., 2018</i>)	NA	https://www.cgl.ucsf.edu/chimerax/
Software, algorithm	UCSF Chimera	(<i>Pettersen et al., 2004</i>)	NA	https://www.cgl.ucsf.edu/chimera
Software, algorithm	PHENIX	(<i>Adams et al., 2010</i>)	NA	https://www.phenix-online.org/
Software, algorithm	Phaser-MR	(<i>McCoy et al., 2007</i>)	NA	https://www.phenix-online.org/documentation/tutorials/mr.html
Software, algorithm	COOT	(<i>Emsley et al., 2010a</i>)	NA	https://www2.mrc-lmb.cam.ac.uk/personal/pemsley/cool
Software, algorithm	MolProbity	(<i>Chen et al., 2010</i>)	NA	http://www.ks.uiuc.edu/Research/mdff/
Software, algorithm	PRIMUS	(<i>Konarev et al., 2003</i>)	NA	https://www.embl-hamburg.de/biosaxs/primus.html
Software, algorithm	CRY SOL	(<i>Svergun et al., 1995</i>)	NA	https://www.embl-hamburg.de/biosaxs/crysol.html
Software, algorithm	GNOM	(<i>Svergun, 1992</i>)	NA	https://www.embl-hamburg.de/biosaxs/gnom.html
Software, algorithm	SEQUEST/Proteome Discoverer Software	ThermoFisher Scientific	NA	https://www.thermofisher.com/order/catalog/product/OPTON-30795
Software, algorithm	HDEXaminer	Sierra Analytics	NA	http://massspec.com/hdexaminer/

Protein

Wild-type human IDE, cysteine-free IDE (IDE-CF), and catalytically inactive IDE mutant, IDE-CF-E111Q were expressed in *E. coli* BL21 (DE3) cells (at 25°C and 20 hr, 0.5 mM IPTG induction using T7 medium). His-tagged, biotinylated IDE was expressed in *E. coli* BL21 (DE3) that carried two plasmids, one for IDE with an N-terminal His-tag and a C-terminal AviTag (GLNDIFEAQKIEWHE), and the other for *E. coli* BirA, a biotin ligase that transfers biotin to AviTag. Recombinant IDE proteins were purified by Ni-NTA, source-Q, and Superdex 200 columns as previously described (*Manolopoulou et al., 2009*). Aβ₁₋₄₀ was synthesized at a 0.25 mmol scale using Fmoc and HBTU/HOBt chemistry on an Applied Biosystems 433A instrument and purified by RP-HPLC, lyophilized, and stored at -20°C under Argon as described (*King et al., 2014; Sohma et al., 2004*). Insulin was purchased from SIGMA (91077C).

IDE-binding synthetic antibody

We screened antigen-binding fragments (Fab) from a phage-display library using immobilized biotinylated IDE as previously described (Miller *et al.*, 2012). To obtain Fabs binding to an epitope distinct from the previously reported IDE-Fab named Fab1 (McCord *et al.*, 2013), we used 1 μ M Fab1 as a competitor for panning in the final round of selection. In total, 18 new IDE binding Fabs were isolated and characterized. Of those, IDE-Fab_{H11} was used in structural studies. Elbow-enhanced Fab1 (Fab1_E) and Fab_{H11-E} were engineered to modify the switch residue region of the Fab heavy chain (wild-type sequence: ¹⁰⁹VTVSSASTKGP¹¹⁹) to VTFVFNQIKGP (Bailey *et al.*, 2018). Fabs were expressed in *E. coli* strain BL21(DE3) or 55244 and purified using a HiTrap protein-G HP column or Protein-G-A1 column as described (Bailey *et al.*, 2014; McCord *et al.*, 2013). Surface plasmon resonance measurements were carried out at 20°C on a Biacore 3000 by immobilizing His-tagged IDE onto a Ni-NTA chip (GE Healthcare) and then injecting 3.3–100 nM of the Fab at a flow rate of 30 μ l/min as previously described (Koide *et al.*, 2012; Zhang *et al.*, 2012).

Enzymatic activity assays

A fluorogenic bradykinin-mimetic substrate of IDE, substrate V (7-methoxycoumarin-4-yl-acetyl-RPPGF-SAFK-2,4-dinitrophenyl, R and D Systems), was used to measure the enzymatic activity of IDE on a Tecan Safire microplate reader using an excitation wavelength of 327 nm and emission wavelength of 395 nm (McCord *et al.*, 2013). Reactions were carried out at 37°C, using 5 μ M substrate V in 100 μ l of 50 mM potassium phosphate (pH 7.3) with the addition of 0.6 nM IDE in the presence or absence of 12 nM Fab_{H11}. The degradation of substrate V was assessed by monitoring fluorescence increase and the initial velocity was calculated using linear regression after background subtraction. The standard deviation was derived from three individual experiments.

Crystallography

IDE-CF-E111Q was first incubated with A β or insulin in a 1:10 or 1:2 ratio, respectively, at 18°C overnight (~16–18 hr) and IDE-substrate complex was purified using Superdex 200 column. This process was repeated three times. Substrate-bound IDE was then mixed in an equimolar ratio with Fab1 or Fab1_E and substrate- and Fab-bound IDE was purified using Superdex 200 column. The resulting complexes were crystallized in 0.1M sodium cacodylate (pH6.5), 0.2M MgCl₂, 10% PEG-3000, and 0.01% ethyl acetate at 18°C by hanging drop vapor diffusion. Crystals formed within 2–3 days. To crystallize Fab_(H11-E)-bound IDE, IDE-CF was purified by Superdex 200 three times before mixing with extra molar Fab_{H11-E} and Fab_{H11-E}-bound IDE was purified by Superdex 200. Such protein complex was crystallized in 0.088M Ammonium citrate tribasic, pH 7, 10% w/v PEG3350, 0.02M ethylenediaminetetraacetic disodium salt dihydrate at 18°C by hanging drop vapor diffusion. Crystals formed in about a week. For data collection, crystals were equilibrated in reservoir buffer with 30% glycerol and flash frozen in liquid nitrogen. Diffraction data were collected at 100K on the 19-ID beamline at Argonne National Laboratory. Data sets were processed using HKL2000 and the CCP4 suite. The structures were determined by molecular replacement. For substrate-bound Fab1-bound IDE structure, the unbound IDE-Fab₁ complex (4IOF) was used as a search model and no NCS average for C2 symmetry of IDE dimer was applied during the refinement to avoid the bias. For the crystal structure of Fab_{H11-E}-bound IDE, the closed-state IDE (2WBY) and Fab in unbound IDE-Fab₁ complex (4IOF) were used as the search model. Model building and refinement were performed by using REFMAC, PHENIX, and COOT (Adams *et al.*, 2011; Emsley *et al.*, 2010b; Potterton *et al.*, 2002). The final model for A β -IDE-Fab1 (pdb = 4M1C) has $R_{\text{work}} = 23\%$ and $R_{\text{free}} = 27\%$, that for Insulin-IDE-Fab1 (pdb = 5 WOB) has $R_{\text{work}} = 24\%$ and $R_{\text{free}} = 29\%$ and that for IDE-Fab_{H11-E} (pdb = 5 UOC) has $R_{\text{work}} = 22\%$ and $R_{\text{free}} = 27\%$. The data and refinement statistics are listed on [Supplementary file 1](#). The key residues involving in the interaction of IDE with Fab_{H11-E} was calculated using PDBePISA (Krissinel and Henrick, 2007).

CryoEM

Purified wild-type IDE was further purified by Superdex 200 chromatography using buffer containing 20 mM HEPES, pH 7.2, 300 mM NaCl, and 20 mM EDTA and then mixed with Fab_{H11-E} at an equal molar ratio. Fab_{H11-E}-IDE complex was purified by Superdex 200 chromatography in the absence or presence of five-fold molar excess of insulin. Insulin-bound IDE-Fab_{H11-E} and IDE-Fab_{H11-E} cryoEM

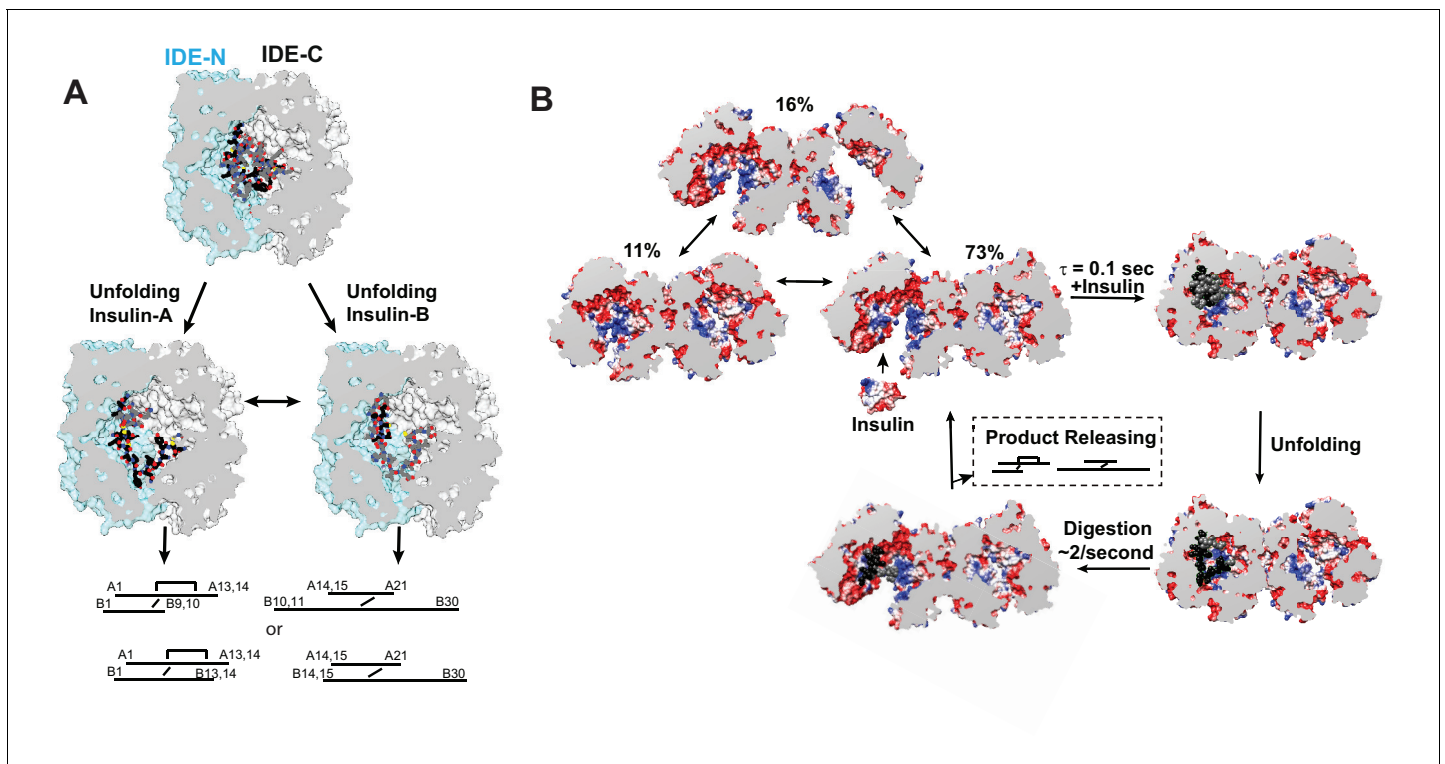
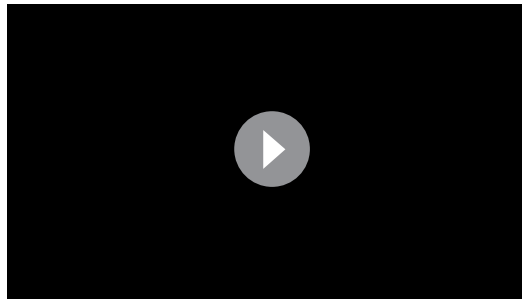


Figure 8. Models for IDE catalytic cycle. (A) Model for conformational changes of insulin inside IDE chamber. Structure of partially unfolded insulin at the IDE catalytic chamber is from PDB code 2WBY while those with unfolded insulin are from PDB code 6B3Q and 6BFC for insulin A and B chain at IDE catalytic site. (B) A model for IDE conformational states relevant to substrate capture and catalysis. For simplicity, only the capture and catalysis of the dominant IDE conformational state, pO/O, is shown. The conformational change of the other IDE subunit allosterically regulated by insulin binding to the open-state IDE within an IDE dimer depicted by **Video 3** is not shown. The electrostatic surface potential of IDE is set from -5 kT/e (red) to 5 kT/e (blue) and calculated by UCSF Chimera, and the section interface is colored as grey.

DOI: <https://doi.org/10.7554/eLife.33572.035>

grids were prepared using either a manual plunger or Spotiton 1.0 (Dandey et al., 2018; Razinkov et al., 2016). For manual plunging, 300 mesh carbon or gold lacey grids, prepared in house (Fukami and Adachi, 1965), were plasma cleaned using O_2 and H_2 for 30 s using a Solarus plasma cleaner (Gatan). 3 μ l of sample was applied to the grid and manually blotted with filter paper for 3 s from the back of the grids followed immediately by plunging into liquid ethane. For Spotiton prepared grids, 300 mesh carbon or gold lacey nanowire grids were plasma cleaned with O_2 and H_2 for 10 secs using a Solarus plasma cleaner (Gatan). 6 μ l of protein sample was aspirated by the Spotiton piezo tip and about 80×50 μ l of sample was delivered to the grid as it passes the piezo tip en route to being plunged into liquid ethane. All images were acquired using a Titan Krios microscope (FEI) operated at 300KeV with a Gatan K2 direct electron detector (Gatan) in counting mode. Images were automatically acquired using Leginon (Suloway et al., 2005) using collection parameters as shown in **Supplementary file 2**. IDE-Fab_{H11-E} showed highly preferred orientation in vitreous ice. Thus, images were acquired with the grid tilted at an angle to the electron beam, which allowed better sampling of other orientations (Figure 2—figure supplement 9B) (Tan et al., 2017). Images were processed using software integrated into the Appion (Lander et al., 2009) pipeline except where stated. Frames were aligned using MotionCor2 software with dose weighting (Zheng et al., 2017), particles were picked and extracted automatically using DoGpicker (Voss et al., 2009). Particle stacks were then passed to RELION2.1 (Scheres, 2012) and processed through several rounds of 2D and 3D classification. Example images and 2D class averages are shown in Figure 2—figure supplements 5–7. Selected classes were then processed for high resolution 3D refinement (Figure 2—figure supplement 8). The resolution was further improved by focused classification with signal subtraction. The mask was created in Chimera (Pettersen et al., 2004) with the Fab regions set to value



Video 3. Morph between IDE conformational states to depict the possible transition between various conformational states of IDE. Only a few synchronized motions are depicted in such morph. Uncoordinated motions between two IDE subunits are not depicted even though they likely occur as well. Scheme 1: Morph to depict synchronized motion of IDE that one IDE subunit undergoes the transition from the open state to the partially open state while the other undergoes the transition in the opposite direction (from the partially open state to the open state). Scheme 2: Morph to depict synchronized motion of IDE that both IDE subunits undergoes the transition between the open state and the partially open state simultaneously. Scheme 3: Morph to depict synchronized motion of IDE that both IDE subunits undergoes the transition between the partially-open state and the partially closed state simultaneously. Scheme 4: Morph to depict synchronized motion of IDE that IDE subunits simultaneously undergoes the transition between the partially-open state, the closed state, and the partially closed state. We hypothesize that IDE undergoes such motion when its substrates are entrapped inside the catalytic chamber. Such motion would allow substrate unfolding, leading the substrate-assisted catalysis.

DOI: <https://doi.org/10.7554/eLife.33572.036>

2M NaCl and then dialyzed against 500 ml 20 mM Tris pH8.0, 100 mM NaCl, 20 mM EDTA and subsequently purified by Superdex 200 column using the buffer containing 20 mM Tris, pH 8.0, 100 mM NaCl, 20 mM EDTA. Greater than 15 measurements around IDE protein peak were collected in each run for subsequent analysis. Time-resolved SAXS experiments were done using a microfluidic laminar flow mixer adapted from the design initially made for time resolved fluorescence studies (Park et al., 2008; Park et al., 2006). The mixer chip consisted of 5 inlets: a center channel for IDE solution, two diagonal channels for identical buffers as the IDE solution and two side channels for buffer containing insulin. Syringe pumps (Model 511, New Era Pump Systems Inc., NY) were used to inject sample and buffer solutions continuously into the mixer inlets. Per measurement, 5–10 mg IDE injected from the center channel were compressed into a thin sheet by the diagonal and side channel flows as a result of the hydrodynamic focusing effect. Kinetic reaction was triggered by diffusion of twofold molar excess of insulin into the jet of IDE from adjacent flow layers of buffer above and below. The thickness of the sheet was controlled by the flow rate ratios of the inlet channels. The observation channel is 1 mm deep (i.e. X-ray pathlength), 0.2 mm wide and 25 mm long. During the flow experiment, the observation channel was sampled by a grid scan of 10×30 positions and SAXS data was collected at each grid point. The total flow rate determined the maximum accessible time corresponding to the exit end of the observation channel. The time window of 2 s was performed by using the flow rates of 68, 2, 9 $\mu\text{L}/\text{min}$ for side, diagonal and center syringe

zero and outside Fab regions set to value one. Subsequently the masked refinement was carried out with C1 symmetry using RELION 2.1 (Scheres, 2012). The final resolution was estimated using Fourier Shell Correlation (FSC = 0.143) in RELION 2.1 (Figure 2—figure supplement 9C and D). The anisotropy was analyzed using 3DFSC (Tan et al., 2017). The cryoEM data collection and processing statistics are listed in Supplementary file 2. The structural models were built using a combination of high-resolution IDE dimer structure (PDB = 2 cww) and Fab_{H11-E}-bound IDE dimer. The density fitting and structure refinement was done using UCSF CHIMERA (Pettersen et al., 2004), COOT (Emsley and Cowtan, 2004; Emsley et al., 2010b), and PHENIX (Adams et al., 2011). The refinement statistics are listed in Supplementary file 3.

SAXS

SAXS data were collected at the BioCAT/18ID beamline at Advanced Photon Source, Argonne National Laboratory (Chicago, USA) (Fischetti et al., 2004) using the photon counting PILATUS 3 1M at room temperature (23°C) and an incident X-ray wavelength of 1.03 Å. The 3.5 m sample-to-detector distance yielded a range of 0.005–0.33 Å⁻¹ for the momentum transfer ($q = 4\pi \sin\theta/\lambda$ where 2θ is the scattered angle between the incident and scattered beam and λ the X-ray wavelength). For size exclusion chromatography (SEC)-SAXS, 2–3 mg IDE was loaded onto a GE Superdex 200 10/300G in the buffer containing 20 mM Tris, pH 8.0, 100 mM NaCl and the eluates were immediately passed through X-ray beam. To prepare zinc-free catalytic inactive IDE, IDE was first washed with about

pumps, respectively. Increasing the flow rates to 682, 22 and 90 $\mu\text{L}/\text{min}$ allows the kinetic study in the time window shorter than 0.2 s. We did three mixing experiments: i) IDE bound with insulin mixing with insulin buffer; ii) IDE mixing with insulin free buffer; and iii) IDE mixing with buffer containing insulin. The mixing experiments i and ii were done using flow rates for 2 s time window while the experiment iii was done for both 2 s and 0.2 s time windows. The SAXS data reduction and analyses were done using ATSAS package (Petoukhov *et al.*, 2012), PRIMUS (Konarev *et al.*, 2003) and CRY SOL (Svergun *et al.*, 1995). Comparison of experimental scattering profiles with calculated profiles from high-resolution atomic models was done using CRY SOL (Svergun *et al.*, 1995). For time-resolved experiments, in order to reduce the effects of the varied parasitic scattering in grid scans, radius of gyration values were obtained using the program GNOM (Petoukhov *et al.*, 2012).

Hydrogen-deuterium exchange mass spectrometry

Prior to carrying out hydrogen/deuterium exchange experiments, the optimal quench condition that generated the best sequence coverage map of IDE were established as previously described (Marsh *et al.*, 2013). IDE stock solutions were prepared in 8.3 mM Tris-HCl, 50 mM NaCl, 2.1% DMSO, pH 7.2 H₂O buffer by mixing 15 μM of IDE with 30 μM Fab_{H11-E}, 150 μM of Insulin, 150 μM of 6bk, 150 μM of BDM44768 or 300 μM of A β , incubating at room temperature for 30 min, then keep on ice for 15 min. Functional hydrogen-deuterium exchange reactions were initiated by dilution of 3 μl of stock solution into 9 μl of D₂O buffer (8.3 mM Tris, 50 mM NaCl, pDREAD 7.2) and incubation at 0°C. The exchange reactions were quenched after various exchange time points (10, 100, 1000, 10,000, 100,000 s at 0°C, and 100,000 s at RT) by adding 18 μl of ice-cold 0.8% formic acid, 1.6M GuHCl, 16.6% glycerol for a final pH of 2.5. Quenched samples were then immediately frozen on dry ice and stored at -80°C before LC/MS analysis. Non-deuterated and equilibrium-deuterated control samples are also prepared as previously described (Tsalkova *et al.*, 2012). The frozen samples were thawed automatically on a cryogenic autosampler (Woods and Hamuro, 2001) at 4°C, and digested on an immobilized pepsin column (16 μl bed volume). Proteolytic products were collected on a C18 trap column (Michrom Magic C18 AQ 0.2 \times 1 mm) for 1 min desalting and separated using a reverse phase analytical column (Michrom Magic C18 AQ 0.2 \times 50 mm, 3 μm) with a acetonitrile linear gradient (6.4%–38.4% over 30 min). MS analysis was performed on an Orbitrap Elite Mass Spectrometer (ThermoFisher Scientific, San Jose, CA). Instruments settings was optimized to minimize the back-exchange (Walters *et al.*, 2012). The data was acquired in both data-dependent MS/MS mode and MS1 profile mode and Proteome Discoverer software (ThermoFisher) was used to identify proteolytic peptides. The deuterium content of the peptides for each time point was calculated by DXMS Explorer (Sierra Analytics Inc, Modesto, CA), with corrections for back-exchange (Zhang and Smith, 1993). H/D exchange experiments performed using our automated system typically produce deuterium incorporation measurements with a standard deviation of less than 2% of the mean of triplicate determinations (Chang *et al.*, 2015; Hsu *et al.*, 2009a; Hsu *et al.*, 2009b). In the present work, just as in our previous studies, only changes in deuteration level greater than 10% were considered significant (Burke *et al.*, 2009; Hamuro *et al.*, 2004). Heat maps were created using in house program that sub-localize HDX down to smaller fragments using all overlapping peptides.

Data and software availability

The cryoEM maps have been deposited in the Electron Microscopy Data Bank with accession codes EMD-7041, EMD-7092, EMD-7065, EMD-7090, EMD-7062, EMD-7093, EMD-7066, and EMD-7091. The atomic models have been deposited in the Protein Data Bank under accession code EMDB 6B3Q, 6BFC, 6BF8, 6B7Y, 6BF6, 6B70, 6BF9, 6B7Z and 6BF7. The crystal structures of Fab1-bound IDE in complex with insulin or A β have been deposited in the Protein Data Bank under access code 5WOB and 4M1C, respectively. The crystal structure of Fab₁-bound IDE in complex with insulin and Fab_{1E} has been deposited in the Protein Data Bank under access code 5CJO. The crystal structures of IDE in complex with Fab_{H11-E} has been deposited in the Protein Data Bank under access code 5UOE.

Acknowledgements

We are grateful to Ryan M Hoffman in Andrew Ward's lab at the Scripps Research Institute for initial negative stained EM data acquisition and analysis, to Srinivas Chakravarthy at BioCAT, APS for assisting with SAXS data collection and analysis, to Juan P Maianti for synthesizing 6bK, and to Steve Meredith for synthetic A β . This work was supported by the NIH grants GM81539 and GM121964 to Wei-Jen Tang, GM103310 to Bridget Carragher and Clinton S Potter, Agency for Science, Technology and Research Singapore to Yong Zi Tan, GM103622 to Tom Irving at BioCAT, APS, and DARPA Fold Fx program (N66001-14-2-4053), NIH R35 GM118062, and the Howard Hughes Medical Institute to David Liu. The Simons Electron Microscopy Center is supported by a grant from the Simons Foundation (349247). Use of the Advanced Photon Source was supported by the U.S. Department of Energy, Office of Basic Energy Sciences, under contract No. DE-AC02-06CH11357.

Additional information

Funding

Funder	Grant reference number	Author
Agency for Science, Technology and Research		Yong Zi Tan
Defense Advanced Research Projects Agency	N66001-14-2-4053	David R Liu
National Institutes of Health	R35 GM118062	David R Liu
Howard Hughes Medical Institute		David R Liu
Simons Foundation	349247	Bridget Carragher Clinton S Potter
National Institutes of Health	GM103310	Bridget Carragher Clinton S Potter
National Institutes of Health	GM81539	Wei-Jen Tang
National Institutes of Health	GM121964	Wei-Jen Tang

The funders had no role in study design, data collection and interpretation, or the decision to submit the work for publication.

Author contributions

Zhenying Zhang, Conceptualization, Data curation, Formal analysis, Investigation, Methodology, Writing—original draft, Writing—review and editing, Performed EM grid preparation, data acquisition and processing; Wenguang G Liang, Conceptualization, Data curation, Formal analysis, Investigation, Methodology, Writing—original draft, Writing—review and editing, Purified protein for EM and conducted negative stained EM data acquisition, Built and refined cryoEM structural models, Performed protein purification and crystallographic data collection, Built and refined structural models, Performed protein purification for HDX-MS, Purified proteins for SAXS studies, Performed SAXS studies; Lucas J Bailey, Data curation, Formal analysis, Investigation, Methodology, Writing—original draft, Writing—review and editing, Screened, purified, and engineered Fab; Yong Zi Tan, Data curation, Formal analysis, Investigation, Methodology, Writing—review and editing, Assisted with EM grid preparation, data acquisition and processing; Hui Wei, Formal analysis, Investigation, Methodology, Assisted with EM grid preparation, data acquisition and processing; Andrew Wang, Data curation, Formal analysis, Writing—review and editing, Built and refined structural models, Performed HDX-MS and analysis; Mara Farcasanu, Data curation, Formal analysis, Investigation, Writing—review and editing, Built and refined structural models; Virgil A Woods, Data curation, Formal analysis; Lauren A McCord, Data curation, Formal analysis, Investigation, Performed protein purification and crystallographic data collection, Built and refined structural models; David Lee, Data curation, Formal analysis, Performed HDX-MS and analysis, Provided critical reagents; Weifeng Shang, Data curation, Formal analysis, Performed SAXS studies; Rebecca Deprez-Poulain, Benoit Deprez, Akiko Koide,

Shohei Koide, Anthony A Kossiakoff, Resources, Provided critical reagents; David R Liu, Resources, Performed HDX-MS and analysis, Provided critical reagents; Sheng Li, Resources, Data curation, Formal analysis, Supervision, Validation, Investigation, Visualization, Methodology, Writing—original draft, Writing—review and editing, Designed the project, Performed HDX-MS and analysis; Bridget Carragher, Clinton S Potter, Conceptualization, Resources, Formal analysis, Supervision, Funding acquisition, Validation, Investigation, Visualization, Writing—original draft, Writing—review and editing, Designed the project, Oversaw EM grid preparation, data acquisition and processing; Wei-Jen Tang, Conceptualization, Resources, Data curation, Formal analysis, Supervision, Funding acquisition, Validation, Investigation, Visualization, Methodology, Writing—original draft, Project administration, Writing—review and editing, Designed the project, Built and refined cryoEM structural models, Built and refined structural models

Author ORCIDs

Yong Zi Tan  <http://orcid.org/0000-0001-6656-6320>

Bridget Carragher  <https://orcid.org/0000-0002-0624-5020>

Clinton S Potter  <https://orcid.org/0000-0003-2394-0831>

Wei-Jen Tang  <https://orcid.org/0000-0002-8267-8995>

Decision letter and Author response

Decision letter <https://doi.org/10.7554/eLife.33572.085>

Author response <https://doi.org/10.7554/eLife.33572.086>

Additional files

Supplementary files

- Supplementary file 1. Data collection and structure refinement statistics

DOI: <https://doi.org/10.7554/eLife.33572.037>

- Supplementary file 2. CryoEM data collection and processing statistic

DOI: <https://doi.org/10.7554/eLife.33572.038>

- Supplementary file 3. CryoEM map and model refinement statistics

DOI: <https://doi.org/10.7554/eLife.33572.039>

- Supplementary file 4. Distances and angles between center of mass of different domains of IDE cryoEM and crystal structures.

DOI: <https://doi.org/10.7554/eLife.33572.040>

- Transparent reporting form

DOI: <https://doi.org/10.7554/eLife.33572.041>

Major datasets

The following datasets were generated:

Author(s)	Year	Dataset title	Dataset URL	Database, license, and accessibility information
Tang WJ	2018	IDE with insulin map	http://www.ebi.ac.uk/pdbe/entry/emdb/EMD-7041	Publicly available at the Electron Microscopy Data Bank (accession no. EMD-7041)
Tang WJ	2018	IDE Open(O)/partial-Open(pO) state map	http://www.ebi.ac.uk/pdbe/entry/emdb/EMD-7092	Publicly available at the Electron Microscopy Data Bank (accession no. EMD-7092)
Tang WJ	2018	IDE O/O state map	http://www.ebi.ac.uk/pdbe/entry/emdb/EMD-7065	Publicly available at the Electron Microscopy Data Bank (accession no. EMD-7065)

Tang WJ	2018	IDE pO/pO state map	http://www.ebi.ac.uk/pdbe/entry/emdb/EMD-7090	Publicly available at the Electron Microscopy Data Bank (accession no. EMD-7090)
Tang WJ	2018	IDE with insulin and FabH11-E map	http://www.ebi.ac.uk/pdbe/entry/emdb/EMD-7062	Publicly available at the Electron Microscopy Data Bank (accession no. EMD-7062)
Tang WJ	2018	IDE O/pO state with FabH11-E map	http://www.ebi.ac.uk/pdbe/entry/emdb/EMD-7093	Publicly available at the Electron Microscopy Data Bank (accession no. EMD-7093)
Tang WJ	2018	IDE O/O state with FabH11-E map	http://www.ebi.ac.uk/pdbe/entry/emdb/EMD-7066	Publicly available at the Electron Microscopy Data Bank (accession no. EMD-7066)
Tang WJ	2018	IDE pO/pO state with FabH11-E map	http://www.ebi.ac.uk/pdbe/entry/emdb/EMD-7091	Publicly available at the Electron Microscopy Data Bank (accession no. EMD-7091)
Tang WJ	2018	IDE with mostly insulin A chain model	http://www.ebi.ac.uk/pdbe/entry/pdb/6b3q	Publicly available at the Electron Microscopy Data Bank (accession no. 6b3q)
Tang WJ	2018	IDE with mostly insulin B chain model	http://www.ebi.ac.uk/pdbe/entry/pdb/6bfc	Publicly available at the Electron Microscopy Data Bank (accession no. 6BFC)
Tang WJ	2018	IDE O/pO state model	http://www.ebi.ac.uk/pdbe/entry/pdb/6bf8	Publicly available at the Electron Microscopy Data Bank (accession no. 6bf8)
Tang WJ	2018	IDE O/O state model	http://www.ebi.ac.uk/pdbe/entry/pdb/6b7y	Publicly available at the Electron Microscopy Data Bank (accession no. 6b7y)
Tang WJ	2018	IDE pO/pO state model	http://www.ebi.ac.uk/pdbe/entry/pdb/6bf6	Publicly available at the Electron Microscopy Data Bank (accession no. 6bf6)
Tang WJ	2018	IDE with insulin and FabH11-E model	http://www.ebi.ac.uk/pdbe/entry/pdb/6b70	Publicly available at the Electron Microscopy Data Bank (accession no. 6b70)
Tang WJ	2018	IDE O/pO state with FabH11-E model	http://www.ebi.ac.uk/pdbe/entry/pdb/6bf9	Publicly available at the Electron Microscopy Data Bank (accession no. 6bf9)
Tang WJ	2018	IDE O/O state with FabH11-E model	http://www.ebi.ac.uk/pdbe/entry/pdb/6b7z	Publicly available at the Electron Microscopy Data Bank (accession no. 6b7z)

Tang WJ	2018	IDE pO/pO state with FabH11-E model	http://www.ebi.ac.uk/pdbe/entry/pdb/6bf7	Publicly available at the Electron Microscopy Data Bank (accession no. 6bf7)
Tang WJ	2018	IDE with insulin and Fab1 structure	http://www.rcsb.org/pdb/search/structid-Search.do?structureId=5WOB	Publicly available at the RCSB Protein Data Bank (accession no. 5WOB)
Tang WJ	2018	IDE with amyloid β and Fab1 structure	https://www.rcsb.org/structure/4M1C	Publicly available at the RCSB Protein Data Bank (accession no. 4M1C)
Tang WJ	2018	IDE with insulin and Fab1E structure	https://www.rcsb.org/structure/5CJO	Publicly available at the RCSB Protein Data Bank (accession no. 5CJO)
Tang WJ	2018	IDE with FabH11-E structure	https://www.rcsb.org/structure/5UOE	Publicly available at the RCSB Protein Data Bank (accession no. 5UOE)

References

- Adames N**, Blundell K, Ashby MN, Boone C. 1995. Role of yeast insulin-degrading enzyme homologs in propheromone processing and bud site selection. *Science* **270**:464–467. DOI: <https://doi.org/10.1126/science.270.5235.464>, PMID: 7569998
- Adams PD**, Afonine PV, Bunkóczi G, Chen VB, Davis IW, Echols N, Headd JJ, Hung LW, Kapral GJ, Grosse-Kunstleve RW, McCoy AJ, Moriarty NW, Oeffner R, Read RJ, Richardson DC, Richardson JS, Terwilliger TC, Zwart PH. 2010. PHENIX: a comprehensive Python-based system for macromolecular structure solution. *Acta Crystallographica Section D Biological Crystallography* **66**:213–221. DOI: <https://doi.org/10.1107/S0907444909052925>, PMID: 20124702
- Adams PD**, Afonine PV, Bunkóczi G, Chen VB, Echols N, Headd JJ, Hung LW, Jain S, Kapral GJ, Grosse-Kunstleve RW, McCoy AJ, Moriarty NW, Oeffner R, Read RJ, Richardson DC, Richardson JS, Terwilliger TC, Zwart PH. 2011. The Phenix software for automated determination of macromolecular structures. *Methods* **55**:94–106. DOI: <https://doi.org/10.1016/j.ymeth.2011.07.005>, PMID: 21821126
- Bailey LJ**, Sheehy KM, Dominik PK, Liang WG, Rui H, Clark M, Jaskolowski M, Kim Y, Deneka D, Tang WJ, Kossiakoff AA. 2018. Locking the Elbow: Improved antibody fab fragments as chaperones for structure determination. *Journal of Molecular Biology* **430**:337–347. DOI: <https://doi.org/10.1016/j.jmb.2017.12.012>, PMID: 29273204
- Bailey LJ**, Sheehy KM, Hoey RJ, Schaefer ZP, Ura M, Kossiakoff AA. 2014. Applications for an engineered Protein-G variant with a pH controllable affinity to antibody fragments. *Journal of Immunological Methods* **415**:24–30. DOI: <https://doi.org/10.1016/j.jim.2014.10.003>, PMID: 25450256
- Blanchet CE**, Svergun DI. 2013. Small-angle X-ray scattering on biological macromolecules and nanocomposites in solution. *Annual Review of Physical Chemistry* **64**:37–54. DOI: <https://doi.org/10.1146/annurev-physchem-040412-110132>, PMID: 23216378
- Burke JE**, Babakhani A, Gorfe AA, Kokotos G, Li S, Woods VL, McCammon JA, Dennis EA. 2009. Location of inhibitors bound to group IVA phospholipase A2 determined by molecular dynamics and deuterium exchange mass spectrometry. *Journal of the American Chemical Society* **131**:8083–8091. DOI: <https://doi.org/10.1021/ja900098y>, PMID: 19459633
- Chang YG**, Cohen SE, Phong C, Myers WK, Kim YI, Tseng R, Lin J, Zhang L, Boyd JS, Lee Y, Kang S, Lee D, Li S, Britt RD, Rust MJ, Golden SS, LiWang A. 2015. Circadian rhythms. A protein fold switch joins the circadian oscillator to clock output in cyanobacteria. *Science* **349**:324–328. DOI: <https://doi.org/10.1126/science.1260031>, PMID: 26113641
- Chen VB**, Arendall WB, Headd JJ, Keedy DA, Immormino RM, Kapral GJ, Murray LW, Richardson JS, Richardson DC. 2010. MolProbity: all-atom structure validation for macromolecular crystallography. *Acta Crystallographica Section D Biological Crystallography* **66**:12–21. DOI: <https://doi.org/10.1107/S0907444909042073>, PMID: 20057044
- Chiti F**, Dobson CM. 2006. Protein misfolding, functional amyloid, and human disease. *Annual Review of Biochemistry* **75**:333–366. DOI: <https://doi.org/10.1146/annurev.biochem.75.101304.123901>, PMID: 16756495
- Chung KY**, Rasmussen SG, Liu T, Li S, DeVree BT, Chae PS, Calinski D, Kobilka BK, Woods VL, Sunahara RK. 2011. Conformational changes in the G protein Gs induced by the β 2 adrenergic receptor. *Nature* **477**:611–615. DOI: <https://doi.org/10.1038/nature10488>, PMID: 21956331
- Deprez-Poulain R**, Hennuyer N, Bosc D, Liang WG, Enée E, Marechal X, Charton J, Totobenazara J, Berte G, Jahklal J, Verdet T, Dumont J, Dassonneville S, Woitrain E, Gauriot M, Paquet C, Duplan I, Hermant P, Cantrelle FX, Sevin E, et al. 2015a. Catalytic site inhibition of insulin-degrading enzyme by a small molecule

- induces glucose intolerance in mice. *Nature Communications* **6**:8250. DOI: <https://doi.org/10.1038/ncomms9250>, PMID: 26394692
- Duckworth WC**, Bennett RG, Hamel FG. 1998. Insulin degradation: progress and potential. *Endocrine Reviews* **19**:608–624. DOI: <https://doi.org/10.1210/er.19.5.608>, PMID: 9793760
- Durham TB**, Toth JL, Klimkowski VJ, Cao JX, Siesky AM, Alexander-Chacko J, Wu GY, Dixon JT, McGee JE, Wang Y, Guo SY, Cavitt RN, Schindler J, Thibodeaux SJ, Calvert NA, Coghlan MJ, Sindelar DK, Christe M, Kiselyov VV, Michael MD, et al. 2015. Dual Exosite-binding Inhibitors of Insulin-degrading Enzyme Challenge Its Role as the Primary Mediator of Insulin Clearance in Vivo. *Journal of Biological Chemistry* **290**:20044–20059. DOI: <https://doi.org/10.1074/jbc.M115.638205>, PMID: 26085101
- Eisenberg D**, Jucker M. 2012. The amyloid state of proteins in human diseases. *Cell* **148**:1188–1203. DOI: <https://doi.org/10.1016/j.cell.2012.02.022>, PMID: 22424229
- Emsley P**, Cowtan K. 2004. Coot: model-building tools for molecular graphics. *Acta Crystallographica. Section D, Biological Crystallography* **60**:2126–2132. DOI: <https://doi.org/10.1107/S0907444904019158>, PMID: 15572765
- Emsley P**, Lohkamp B, Scott WG, Cowtan K. 2010a. Features and development of Coot. *Acta Crystallographica. Section D, Biological Crystallography* **66**:486–501. DOI: <https://doi.org/10.1107/S0907444910007493>, PMID: 20383002
- Emsley P**, Lohkamp B, Scott WG, Cowtan K. 2010b. Features and development of Coot. *Acta Crystallographica. Section D, Biological Crystallography* **66**:486–501. DOI: <https://doi.org/10.1107/S0907444910007493>, PMID: 20383002
- Dandey VP**, Wei H, Zhang Z, Tan YZ, Acharya P, Eng ET, Rice WJ, Kahn PA, Potter CS, Carragher B. 2018. Spotiton: New features and applications. *Journal of Structural Biology* **202**:161–169. DOI: <https://doi.org/10.1016/j.jsb.2018.01.002>, PMID: 29366716
- Farris W**, Mansourian S, Chang Y, Lindsley L, Eckman EA, Frosch MP, Eckman CB, Tanzi RE, Selkoe DJ, Guenette S. 2003. Insulin-degrading enzyme regulates the levels of insulin, amyloid beta-protein, and the beta-amyloid precursor protein intracellular domain in vivo. *PNAS* **100**:4162–4167. DOI: <https://doi.org/10.1073/pnas.0230450100>, PMID: 12634421
- Farris W**, Mansourian S, Leissring MA, Eckman EA, Bertram L, Eckman CB, Tanzi RE, Selkoe DJ. 2004. Partial loss-of-function mutations in insulin-degrading enzyme that induce diabetes also impair degradation of amyloid beta-protein. *The American Journal of Pathology* **164**:1425–1434. DOI: [https://doi.org/10.1016/S0002-9440\(10\)63229-4](https://doi.org/10.1016/S0002-9440(10)63229-4), PMID: 15039230
- Fischetti R**, Stepanov S, Rosenbaum G, Barrea R, Black E, Gore D, Heurich R, Kondrashkina E, Kropf AJ, Wang S, Zhang K, Irving TC, Bunker GB. 2004. The BioCAT undulator beamline 18ID: a facility for biological non-crystalline diffraction and X-ray absorption spectroscopy at the Advanced Photon Source. *Journal of Synchrotron Radiation* **11**:399–405. DOI: <https://doi.org/10.1107/S0909049504016760>, PMID: 15310956
- Fitzpatrick AWP**, Falcon B, He S, Murzin AG, Murshudov G, Garringer HJ, Crowther RA, Ghetti B, Goedert M, Scheres SHW. 2017. Cryo-EM structures of tau filaments from Alzheimer's disease. *Nature* **547**:185–190. DOI: <https://doi.org/10.1038/nature23002>, PMID: 28678775
- Fuchsberger C**, Flannick J, Teslovich TM, Mahajan A, Agarwala V, Gaulton KJ, Ma C, Fontanillas P, Moutsianas L, McCarthy DJ, Rivas MA, Pery JRB, Sim X, Blackwell TW, Robertson NR, Rayner NW, Cingolani P, Locke AE, Tajos JF, Highland HM, et al. 2016. The genetic architecture of type 2 diabetes. *Nature* **536**:41–47. DOI: <https://doi.org/10.1038/nature18642>, PMID: 27398621
- Fujita A**, Oka C, Arikawa Y, Katagai T, Tonouchi A, Kuhara S, Misumi Y. 1994. A yeast gene necessary for bud-site selection encodes a protein similar to insulin-degrading enzymes. *Nature* **372**:567–570. DOI: <https://doi.org/10.1038/372567a0>, PMID: 7990931
- Fukami A**, Adachi K. 1965. A new method of preparation of a self-perforated micro plastic grid and its application. *Journal of Electron Microscopy* **14**:112–118. PMID: 5852585
- Galagovsky D**, Katz MJ, Acevedo JM, Soriano E, Glavic A, Wappner P. 2014. The Drosophila insulin-degrading enzyme restricts growth by modulating the PI3K pathway in a cell-autonomous manner. *Molecular Biology of the Cell* **25**:916–924. DOI: <https://doi.org/10.1091/mbc.E13-04-0213>, PMID: 24430872
- Goddard TD**, Huang CC, Meng EC, Pettersen EF, Couch GS, Morris JH, Ferrin TE. 2018. UCSF ChimeraX: Meeting modern challenges in visualization and analysis. *Protein Science : A Publication of the Protein Society* **27**. DOI: <https://doi.org/10.1002/pro.3235>, PMID: 28710774
- Guo Q**, Manolopoulou M, Bian Y, Schilling AB, Tang WJ. 2010. Molecular basis for the recognition and cleavages of IGF-II, TGF-alpha, and amylin by human insulin-degrading enzyme. *Journal of Molecular Biology* **395**:430–443. DOI: <https://doi.org/10.1016/j.jmb.2009.10.072>, PMID: 19896952
- Hamuro Y**, Anand GS, Kim JS, Juliano C, Stranz DD, Taylor SS, Woods VL. 2004. Mapping intersubunit interactions of the regulatory subunit (R1alpha) in the type I holoenzyme of protein kinase A by amide hydrogen/deuterium exchange mass spectrometry (DXMS). *Journal of Molecular Biology* **340**:1185–1196. DOI: <https://doi.org/10.1016/j.jmb.2004.05.042>, PMID: 15236976
- Henderson R**. 2015. Overview and future of single particle electron cryomicroscopy. *Archives of Biochemistry and Biophysics* **581**:19–24. DOI: <https://doi.org/10.1016/j.abb.2015.02.036>, PMID: 25796174
- Hsu S**, Kim Y, Li S, Durrant ES, Pace RM, Woods VL, Gentry MS. 2009a. Structural insights into glucan phosphatase dynamics using amide hydrogen-deuterium exchange mass spectrometry. *Biochemistry* **48**:9891–9902. DOI: <https://doi.org/10.1021/bi9008853>, PMID: 19754155
- Hsu YH**, Burke JE, Li S, Woods VL, Dennis EA. 2009b. Localizing the membrane binding region of Group VIA Ca^{2+} -independent phospholipase A2 using peptide amide hydrogen/deuterium exchange mass spectrometry.

- The Journal of Biological Chemistry* **284**:23652–23661. DOI: <https://doi.org/10.1074/jbc.M109.021857>, PMID: 19556238
- Jucker M**, Walker LC. 2013. Self-propagation of pathogenic protein aggregates in neurodegenerative diseases. *Nature* **501**:45–51. DOI: <https://doi.org/10.1038/nature12481>, PMID: 24005412
- Kim J**, Wu S, Tomasiak TM, Mergel C, Winter MB, Stiller SB, Robles-Colmanares Y, Stroud RM, Tampé R, Craik CS, Cheng Y. 2015. Subnanometre-resolution electron cryomicroscopy structure of a heterodimeric ABC exporter. *Nature* **517**:396–400. DOI: <https://doi.org/10.1038/nature13872>, PMID: 25363761
- King JV**, Liang WG, Scherpelz KP, Schilling AB, Meredith SC, Tang WJ. 2014. Molecular basis of substrate recognition and degradation by human presequence protease. *Structure* **22**:996–1007. DOI: <https://doi.org/10.1016/j.str.2014.05.003>, PMID: 24931469
- Koide A**, Wojcik J, Gilbreth RN, Hoey RJ, Koide S. 2012. Teaching an old scaffold new tricks: monobodies constructed using alternative surfaces of the FN3 scaffold. *Journal of Molecular Biology* **415**:393–405. DOI: <https://doi.org/10.1016/j.jmb.2011.12.019>, PMID: 22198408
- Konarev PV**, Volkov VV, Sokolova AV, Koch MHJ, Svergun DI. 2003. PRIMUS : a Windows PC-based system for small-angle scattering data analysis . *Journal of Applied Crystallography* **36**:1277–1282. DOI: <https://doi.org/10.1107/S0021889803012779>
- Krissinel E**, Henrick K. 2007. Inference of macromolecular assemblies from crystalline state. *Journal of Molecular Biology* **372**:774–797. DOI: <https://doi.org/10.1016/j.jmb.2007.05.022>, PMID: 17681537
- Kurochkin IV**, Guarnera E, Berezovsky IN. 2018. Insulin-degrading enzyme in the fight against alzheimer's disease. *Trends in Pharmacological Sciences* **39**:49–58. DOI: <https://doi.org/10.1016/j.tips.2017.10.008>, PMID: 29132916
- Kurochkin IV**. 2001. Insulin-degrading enzyme: embarking on amyloid destruction. *Trends in Biochemical Sciences* **26**:421–425. DOI: [https://doi.org/10.1016/S0968-0004\(01\)01876-X](https://doi.org/10.1016/S0968-0004(01)01876-X), PMID: 11440853
- Lander GC**, Stagg SM, Voss NR, Cheng A, Fellmann D, Pulokas J, Yoshioka C, Irving C, Mulder A, Lau PW, Lyumkis D, Potter CS, Carragher B. 2009. Appion: an integrated, database-driven pipeline to facilitate EM image processing. *Journal of Structural Biology* **166**:95–102. DOI: <https://doi.org/10.1016/j.jsb.2009.01.002>, PMID: 19263523
- Leissring MA**, Farris W, Chang AY, Walsh DM, Wu X, Sun X, Frosch MP, Selkoe DJ. 2003. Enhanced proteolysis of beta-amyloid in APP transgenic mice prevents plaque formation, secondary pathology, and premature death. *Neuron* **40**:1087–1093. DOI: [https://doi.org/10.1016/S0896-6273\(03\)00787-6](https://doi.org/10.1016/S0896-6273(03)00787-6), PMID: 14687544
- Li P**, Kuo WL, Yousef M, Rosner MR, Tang WJ. 2006. The C-terminal domain of human insulin degrading enzyme is required for dimerization and substrate recognition. *Biochemical and Biophysical Research Communications* **343**:1032–1037. DOI: <https://doi.org/10.1016/j.bbrc.2006.03.083>, PMID: 16574064
- Li S**, Tsalkova T, White MA, Mei FC, Liu T, Wang D, Woods VL, Cheng X. 2011. Mechanism of intracellular cAMP sensor Epac2 activation: cAMP-induced conformational changes identified by amide hydrogen/deuterium exchange mass spectrometry (DXMS). *The Journal of Biological Chemistry* **286**:17889–17897. DOI: <https://doi.org/10.1074/jbc.M111.224535>, PMID: 21454623
- Li X**, Mooney P, Zheng S, Booth CR, Braunfeld MB, Gubbens S, Agard DA, Cheng Y. 2013. Electron counting and beam-induced motion correction enable near-atomic-resolution single-particle cryo-EM. *Nature Methods* **10**:584–590. DOI: <https://doi.org/10.1038/nmeth.2472>, PMID: 23644547
- Lu JX**, Qiang W, Yau WM, Schwieters CD, Meredith SC, Tycko R. 2013. Molecular structure of β -Amyloid fibrils in alzheimer's disease brain tissue. *Cell* **154**:1257–1268. DOI: <https://doi.org/10.1016/j.cell.2013.08.035>, PMID: 24034249
- Lyumkis D**, Julien JP, de Val N, Cupo A, Potter CS, Klasse PJ, Burton DR, Sanders RW, Moore JP, Carragher B, Wilson IA, Ward AB. 2013. Cryo-EM structure of a fully glycosylated soluble cleaved HIV-1 envelope trimer. *Science* **342**:1484–1490. DOI: <https://doi.org/10.1126/science.1245627>, PMID: 24179160
- Maianti JP**, McFedries A, Foda ZH, Kleiner RE, Du XQ, Leissring MA, Tang WJ, Charron MJ, Seeliger MA, Saghatelian A, Liu DR. 2014. Anti-diabetic activity of insulin-degrading enzyme inhibitors mediated by multiple hormones. *Nature* **511**:94–98. DOI: <https://doi.org/10.1038/nature13297>, PMID: 24847884
- Malito E**, Hulse RE, Tang WJ. 2008a. Amyloid beta-degrading cryptidases: insulin degrading enzyme, presequence peptidase, and neprilysin. *Cellular and Molecular Life Sciences* **65**:2574–2585. DOI: <https://doi.org/10.1007/s00018-008-8112-4>, PMID: 18470479
- Malito E**, Ralat LA, Manolopoulou M, Tsay JL, Wadlington NL, Tang WJ. 2008. Molecular bases for the recognition of short peptide substrates and cysteine-directed modifications of human insulin-degrading enzyme. *Biochemistry* **47**:12822–12834. DOI: <https://doi.org/10.1021/bi801192h>, PMID: 18986166
- Manolopoulou M**, Guo Q, Malito E, Schilling AB, Tang WJ. 2009. Molecular basis of catalytic chamber-assisted unfolding and cleavage of human insulin by human insulin-degrading enzyme. *Journal of Biological Chemistry* **284**:14177–14188. DOI: <https://doi.org/10.1074/jbc.M900068200>, PMID: 19321446
- Marciano DP**, Dharmarajan V, Griffin PR. 2014. HDX-MS guided drug discovery: small molecules and biopharmaceuticals. *Current Opinion in Structural Biology* **28**:105–111. DOI: <https://doi.org/10.1016/j.sbi.2014.08.007>, PMID: 25179005
- Marsh JJ**, Guan HS, Li S, Chiles PG, Tran D, Morris TA. 2013. Structural insights into fibrinogen dynamics using amide hydrogen/deuterium exchange mass spectrometry. *Biochemistry* **52**:5491–5502. DOI: <https://doi.org/10.1021/bi4007995>, PMID: 23875785
- McCord LA**, Liang WG, Dowdell E, Kalas V, Hoey RJ, Koide A, Koide S, Tang WJ. 2013. Conformational states and recognition of amyloidogenic peptides of human insulin-degrading enzyme. *PNAS* **110**:13827–13832. DOI: <https://doi.org/10.1073/pnas.1304575110>, PMID: 23922390

- McCoy AJ**, Grosse-Kunstleve RW, Adams PD, Winn MD, Storoni LC, Read RJ. 2007. Phaser crystallographic software. *Journal of Applied Crystallography* **40**:658–674. DOI: <https://doi.org/10.1107/S0021889807021206>, PMID: 19461840
- Merk A**, Bartesaghi A, Banerjee S, Falconieri V, Rao P, Davis MI, Pragani R, Boxer MB, Earl LA, Milne JLS, Subramaniam S. 2016. Breaking Cryo-EM Resolution Barriers to Facilitate Drug Discovery. *Cell* **165**:1698–1707. DOI: <https://doi.org/10.1016/j.cell.2016.05.040>, PMID: 27238019
- Merlini G**, Bellotti V. 2003. Molecular mechanisms of amyloidosis. *New England Journal of Medicine* **349**:583–596. DOI: <https://doi.org/10.1056/NEJMra023144>, PMID: 12904524
- Miller KR**, Koide A, Leung B, Fitzsimmons J, Yoder B, Yuan H, Jay M, Sidhu SS, Koide S, Collins EJ. 2012. T cell receptor-like recognition of tumor in vivo by synthetic antibody fragment. *PLoS ONE* **7**:e43746. DOI: <https://doi.org/10.1371/journal.pone.0043746>, PMID: 22916301
- Noiraj N**, Bhasin SK, Song ES, Scoggin KE, Juliano MA, Juliano L, Hersh LB, Rodgers DW. 2011. Identification of the allosteric regulatory site of insulin. *PLoS ONE* **6**:e20864. DOI: <https://doi.org/10.1371/journal.pone.0020864>, PMID: 21731629
- Park HY**, Kim SA, Korlach J, Rhoades E, Kwok LW, Zipfel WR, Waxham MN, Webb WW, Pollack L. 2008. Conformational changes of calmodulin upon Ca²⁺ binding studied with a microfluidic mixer. *PNAS* **105**:542–547. DOI: <https://doi.org/10.1073/pnas.0710810105>, PMID: 18178620
- Park HY**, Qiu X, Rhoades E, Korlach J, Kwok LW, Zipfel WR, Webb WW, Pollack L. 2006. Achieving uniform mixing in a microfluidic device: hydrodynamic focusing prior to mixing. *Analytical Chemistry* **78**:4465–4473. DOI: <https://doi.org/10.1021/ac060572n>, PMID: 16808455
- Petoukhov MV**, Franke D, Shkumatov AV, Tria G, Kikhney AG, Gajda M, Gorba C, Mertens HD, Konarev PV, Svergun DI. 2012. New developments in the ATSAS program package for small-angle scattering data analysis. *Journal of Applied Crystallography* **45**:342–350. DOI: <https://doi.org/10.1107/S0021889812007662>, PMID: 25484842
- Petterson EF**, Goddard TD, Huang CC, Couch GS, Greenblatt DM, Meng EC, Ferrin TE. 2004. UCSF Chimera—a visualization system for exploratory research and analysis. *Journal of Computational Chemistry* **25**:1605–1612. DOI: <https://doi.org/10.1002/jcc.20084>, PMID: 15264254
- Pivovarova O**, Höhn A, Grune T, Pfeiffer AF, Rudovich N. 2016. Insulin-degrading enzyme: new therapeutic target for diabetes and Alzheimer's disease? *Annals of Medicine* **48**:614–624. DOI: <https://doi.org/10.1080/07853890.2016.1197416>, PMID: 27320287
- Potterton E**, McNicholas S, Krissinel E, Cowtan K, Noble M. 2002. The CCP4 molecular-graphics project. *Acta Crystallographica. Section D, Biological Crystallography* **58**:1955–1957. DOI: <https://doi.org/10.1107/S0907444902015391>, PMID: 12393928
- Putnam CD**, Hammel M, Hura GL, Tainer JA. 2007. X-ray solution scattering (SAXS) combined with crystallography and computation: defining accurate macromolecular structures, conformations and assemblies in solution. *Quarterly Reviews of Biophysics* **40**:191–285. DOI: <https://doi.org/10.1017/S0033583507004635>, PMID: 18078545
- Ralat LA**, Guo Q, Ren M, Funke T, Dickey DM, Potter LR, Tang WJ. 2011. Insulin-degrading enzyme modulates the natriuretic peptide-mediated signaling response. *Journal of Biological Chemistry* **286**:4670–4679. DOI: <https://doi.org/10.1074/jbc.M110.173252>, PMID: 21098034
- Razinkov I**, Dandey V, Wei H, Zhang Z, Melnekoff D, Rice WJ, Wigge C, Potter CS, Carragher B. 2016. A new method for vitrifying samples for cryoEM. *Journal of Structural Biology* **195**:190–198. DOI: <https://doi.org/10.1016/j.jsb.2016.06.001>, PMID: 27288865
- Ren M**, Guo Q, Guo L, Lenz M, Qian F, Koenen RR, Xu H, Schilling AB, Weber C, Ye RD, Dinner AR, Tang WJ. 2010. Polymerization of MIP-1 chemokine (CCL3 and CCL4) and clearance of MIP-1 by insulin-degrading enzyme. *The EMBO Journal* **29**:3952–3966. DOI: <https://doi.org/10.1038/emboj.2010.256>, PMID: 20959807
- Russo CJ**, Passmore LA. 2014. Electron microscopy: Ultrastable gold substrates for electron cryomicroscopy. *Science* **346**:1377–1380. DOI: <https://doi.org/10.1126/science.1259530>, PMID: 25504723
- Scheres SH**. 2012. RELION: implementation of a Bayesian approach to cryo-EM structure determination. *Journal of Structural Biology* **180**:519–530. DOI: <https://doi.org/10.1016/j.jsb.2012.09.006>, PMID: 23000701
- Sharma SK**, Chorell E, Steneberg P, Vernersson-Lindahl E, Edlund H, Wittung-Stafshede P. 2015. Insulin-degrading enzyme prevents α -synuclein fibril formation in a nonproteolytic manner. *Scientific Reports* **5**:12531. DOI: <https://doi.org/10.1038/srep12531>, PMID: 26228656
- Shen Y**, Joachimiak A, Rosner MR, Tang WJ. 2006. Structures of human insulin-degrading enzyme reveal a new substrate recognition mechanism. *Nature* **443**:870–874. DOI: <https://doi.org/10.1038/nature05143>, PMID: 17051221
- Sohma Y**, Sasaki M, Hayashi Y, Kimura T, Kiso Y. 2004. Design and synthesis of a novel water-soluble A β 1-42 isopeptide: an efficient strategy for the preparation of Alzheimer's disease-related peptide, A β 1-42, via O–N intramolecular acyl migration reaction. *Tetrahedron Letters* **45**:5965–5968. DOI: <https://doi.org/10.1016/j.tetlet.2004.06.059>
- Song ES**, Juliano MA, Juliano L, Hersh LB. 2003. Substrate activation of insulin-degrading enzyme (insulysin). A potential target for drug development. *The Journal of Biological Chemistry* **278**:49789–49794. DOI: <https://doi.org/10.1074/jbc.M308983200>, PMID: 14527953
- Song ES**, Rodgers DW, Hersh LB. 2010. A monomeric variant of insulin degrading enzyme (IDE) loses its regulatory properties. *PLoS ONE* **5**:e9719. DOI: <https://doi.org/10.1371/journal.pone.0009719>, PMID: 20300529

- Suloway C**, Pulokas J, Fellmann D, Cheng A, Guerra F, Quispe J, Stagg S, Potter CS, Carragher B. 2005. Automated molecular microscopy: the new Legimon system. *Journal of Structural Biology* **151**:41–60. DOI: <https://doi.org/10.1016/j.jsb.2005.03.010>, PMID: 15890530
- Svergun D**, Barberato C, Koch MHJ. 1995. CRY SOL – a Program to Evaluate X-ray Solution Scattering of Biological Macromolecules from Atomic Coordinates. *Journal of Applied Crystallography* **28**:768–773. DOI: <https://doi.org/10.1107/S0021889895007047>
- Svergun DI**. 1992. Determination of the regularization parameter in indirect-transform methods using perceptual criteria. *Journal of Applied Crystallography* **25**:495–503. DOI: <https://doi.org/10.1107/S0021889892001663>
- Tan YZ**, Baldwin PR, Davis JH, Williamson JR, Potter CS, Carragher B, Lyumkis D. 2017. Addressing preferred specimen orientation in single-particle cryo-EM through tilting. *Nature Methods* **14**:793–796. DOI: <https://doi.org/10.1038/nmeth.4347>, PMID: 28671674
- Tang WJ**. 2016. Targeting Insulin-Degrading Enzyme to Treat Type 2 Diabetes Mellitus. *Trends in Endocrinology & Metabolism* **27**:24–34. DOI: <https://doi.org/10.1016/j.tem.2015.11.003>, PMID: 26651592
- Tsalkova T**, Mei FC, Li S, Chepurny OG, Leech CA, Liu T, Holz GG, Woods VL, Cheng X. 2012. Isoform-specific antagonists of exchange proteins directly activated by cAMP. *PNAS* **109**:18613–18618. DOI: <https://doi.org/10.1073/pnas.1210209109>, PMID: 23091014
- Tundo GR**, Sbardella D, Ciaccio C, Grasso G, Gioia M, Coletta A, Polticelli F, Di Pierro D, Milardi D, Van Endert P, Marini S, Coletta M. 2017. Multiple functions of insulin-degrading enzyme: a metabolic crosslight? *Critical Reviews in Biochemistry and Molecular Biology* **52**:554–582. DOI: <https://doi.org/10.1080/10409238.2017.1337707>, PMID: 28635330
- Voss NR**, Yoshioka CK, Radermacher M, Potter CS, Carragher B. 2009. DoG picker and tiltpicker: software tools to facilitate particle selection in single particle electron microscopy. *Journal of Structural Biology* **166**:205–213. DOI: <https://doi.org/10.1016/j.jsb.2009.01.004>, PMID: 19374019
- Walters BT**, Ricciuti A, Mayne L, Englander SW. 2012. Minimizing back exchange in the hydrogen exchange-mass spectrometry experiment. *Journal of the American Society for Mass Spectrometry* **23**:2132–2139. DOI: <https://doi.org/10.1007/s13361-012-0476-x>, PMID: 22965280
- Ward AB**, Sali A, Wilson IA. 2013. Biochemistry. Integrative structural biology. *Science* **339**:913–915. DOI: <https://doi.org/10.1126/science.1228565>, PMID: 23430643
- Wei H**, Mo J, Tao L, Russell RJ, Tymiak AA, Chen G, Iacob RE, Engen JR. 2014. Hydrogen/deuterium exchange mass spectrometry for probing higher order structure of protein therapeutics: methodology and applications. *Drug Discovery Today* **19**:95–102. DOI: <https://doi.org/10.1016/j.drudis.2013.07.019>, PMID: 23928097
- Woods VL**, Hamuro Y. 2001. High resolution, high-throughput amide deuterium exchange-mass spectrometry (DXMS) determination of protein binding site structure and dynamics: Utility in pharmaceutical design. *Journal of Cellular Biochemistry* **84**:89–98. DOI: <https://doi.org/10.1002/jcb.10069>
- Wu S**, Avila-Sakar A, Kim J, Booth DS, Greenberg CH, Rossi A, Liao M, Li X, Alian A, Griner SL, Juge N, Yu Y, Mergel CM, Chaparro-Riggers J, Strop P, Tampé R, Edwards RH, Stroud RM, Craik CS, Cheng Y. 2012. Fabs enable single particle cryoEM studies of small proteins. *Structure* **20**:582–592. DOI: <https://doi.org/10.1016/j.str.2012.02.017>, PMID: 22483106
- Zhang X**, Hoey RJ, Lin G, Koide A, Leung B, Ahn K, Dolios G, Paduch M, Ikeuchi T, Wang R, Li YM, Koide S, Sisodia SS. 2012. Identification of a tetratricopeptide repeat-like domain in the nicastrin subunit of γ -secretase using synthetic antibodies. *PNAS* **109**:8534–8539. DOI: <https://doi.org/10.1073/pnas.1202691109>, PMID: 22586122
- Zhang Z**, Smith DL. 1993. Determination of amide hydrogen exchange by mass spectrometry: a new tool for protein structure elucidation. *Protein Science* **2**:522–531. DOI: <https://doi.org/10.1002/pro.5560020404>, PMID: 8390883
- Zheng S**, Polovcak E, Armache JP, Cheng Y, Agard D. 2017. Anisotropic correction of beam-induced motion for improved single-particle electron cryomicroscopy. *Nature Methods* **14**:331–332. DOI: <https://doi.org/10.1038/nmeth.4193>